Journal of Applied Geophysics 230 (2024) 105540

Contents lists available at ScienceDirect

Journal of Applied Geophysics

journal homepage: www.elsevier.com/locate/jappgeo

Improved sub-ice platelet layer mapping with multi-frequency EM induction sounding

Mara Neudert [a,*], Stefanie Arndt [a,c], Stefan Hendricks [a], Mario Hoppmann [a], Markus Schulze [a], Christian Haas [a,b]

[a] Alfred Wegener Institute, Helmholtz Centre for Polar and Marine Research, Am Handelshafen 12, D-27570 Bremerhaven, Germany
[b] Institute for Environmental Physics, University of Bremen, Otto-Hahn-Allee 1, D-28359 Bremen, Germany
[c] University of Hamburg. Institute of Oceanography, Hamburg, Germany

ARTICLE INFO

Keywords:
Sea ice
Sub-ice platelet layers
Electromagnetic induction sounding
Multi-frequency EM measurements

ABSTRACT

In Antarctica, sub-ice platelet layers (SIPL) accumulate beneath sea ice where ice crystals emerge from adjacent ice shelf cavities, serving as a unique habitat and indicator of ice-ocean interaction. Atka Bay in the eastern Weddell Sea, close to the German overwintering base Neumayer Station III, is well known for hosting a SIPL linked to ice shelf water outflow from beneath the Ekström Ice Shelf. This study presents a comprehensive analysis of an extensive multi-frequency electromagnetic (EM) induction sounding dataset in Atka Bay. Employing an open-source inversion scheme, the dataset was inverted to determine fast ice and platelet layer thicknesses along with their electrical conductivities. From electrical conductivity of the SIPL, we derive the SIPL solid fraction. Our results demonstrate the capability of obtaining high-resolution maps of SIPL thickness over extensive areas, providing unprecedented insights into accumulation patterns and identifying regions of ice-shelf water outflow in Atka Bay. Calibration in a zero-conductivity environment on the ice shelf proves effective, reducing logistical efforts for correcting electronic offsets and drift. Moreover, we demonstrate that both instrument noise and motion noise are sufficiently low to accurately determine SIPL thickness, with uncertainties within the decimeter range. Notably, this investigation is the first to cover the entirety of Atka Bay, including ice shelf fringes, overcoming limitations of prior studies. Our approach represents a significant advancement in studying ocean/ice-shelf interactions using non-destructive EM methods, emphasizing the potential to assess future changes in sub-ice shelf processes. In the future, the adaptation of this method to airborne multi-frequency EM measurements using drones or aircraft has the potential to further extend spatial coverage.

1. Introduction

In numerous coastal fast-ice regions around Antarctica, a sub-ice platelet layer (SIPL) is found below the consolidated ice, typically as a loosely consolidated, highly porous layer composed of planar ice crystals ranging in size from millimeters to decimeters (Hoppmann et al., 2020). The presence of a SIPL stabilises the overlying fast ice system by providing a positive contribution to the ice mass balance (Gough et al., 2012). In Atka Bay, the SIPL reaches a thickness of 4 m on average, and locally up to 10 m at the end of the sea-ice growth season (Arndt et al., 2020; Hunkeler et al., 2016b; Hoppmann et al., 2015b, a). Its presence and thickness are important indicators of the occurrence of Ice Shelf Water (ISW) near the ocean surface (Langhorne et al., 2015), as the presence of ISW is necessary for the creation of platelet ice (Mahoney et al., 2011). ISW forms through melting at the base of ice shelves, and is distinguished by a potential temperature below the surface freezing point, known as potential supercooling (Jacobs, 2004).

The distinctive feature of the SIPL, contrasting consolidated sea ice, lies in its low solid fraction ranging from 0.15 to 0.45, with interstices filled by ambient-temperature seawater (Hoppmann et al., 2020, 2015b; Robinson et al., 2014). Anticipated electrical conductivity of the SIPL ranges between 500 and 1800 mS/m (Haas et al., 2021; Hunkeler et al., 2016b), contrasting with the lower conductivities of overlying consolidated sea ice (0–50 mS/m, Haas et al. (1997)) and the higher conductivity of underlying seawater (2700 mS/m, Haas et al. (2021); Hunkeler et al. (2016b)). Ground-based frequency-domain electromagnetic (EM) induction sounding, employing small-coil instruments, has been applied to investigate SIPL thickness and ice volume fraction in Atka Bay. In

* Corresponding author.
E-mail address: mneudert@awi.de (M. Neudert).

https://doi.org/10.1016/j.jappgeo.2024.105540
Received 11 April 2024; Received in revised form 7 October 2024; Accepted 10 October 2024
Available online 21 October 2024

earlier surveys, Hunkeler et al. (2016a, 2016b) utilized a snowmobile to tow the electromagnetic (EM) instrument on a sled, and we have adopted this method in our own surveys. Still, the comprehensive distribution of SIPL thickness and ice volume fraction across the bay remains poorly understood, as these previous studies were spatially constrained to a small number of profiles. The EM method exploits that the effective electrical conductivity of the SIPL is tied to the solid fraction. In our case, EM responses from this subsurface are characterized using a one-dimensional three-layer model, comprising an "ice+snow" layer and a SIPL above a homogeneous half space with seawater conductivity, under the assumption that sea ice and snow can be treated as a flat, uniform 1D layer, a typical scenario for level fast ice.

In general, the frequency-domain EM response is the measured ratio between secondary and primary field strength, with real (or Inphase) and imaginary (or Quadrature) components at each frequency Wait (1982). This response can be described by a geophysical forward model for horizontal-coplanar (HCP) receiver-transmitter-coil configuration over a horizontally isotropic layered medium Wait (1982). An inverse algorithm is used to iteratively calculate a solution for the free parameters until the minimum misfit between data and model results is reached. By inverting the EM response to sea ice with an underlying SIPL of a single-frequency instrument, one can extract two free parameters, usually the respective layer thicknesses (Brett et al., 2020; Haas et al., 2021), while multi-frequency surveys can simultaneously resolve layer conductivities (Hunkeler et al., 2015, 2016b), making it a non-invasive method for mapping the thickness and ice volume fraction associated with the SIPL. In contrast to other EM near-surface studies, the retrieval of sea ice properties presents distinct challenges primarily due to the exceptionally high conductivity environment near seawater, a condition not typically accommodated by the bucking coil design of commercial instruments like the GEM-2 (Hunkeler et al., 2016a). This limitation can be addressed by integrating a sensor-specific correction for the bucking coil bias (Hunkeler et al., 2016a).

In light of the promising role of geophysics in diverse sea ice investigations, there is a recent demand for adaptable and user-friendly EM inversion software. The availability of open source user-friendly inversion software packages has expanded and we use and modify the API of the Python-based open-source EM induction inversion software, EMagPy (McLachlan et al., 2021). EMagPy has capabilities to generate synthetic data, filter and calibrate field data, and perform quasi-2D/3D inversions (McLachlan et al., 2021).

In practice, accurate quantitative retrieval of ice properties from multi-frequency EM surveys adds challenges related to instrument calibration to deal with systematic offsets and temperature-driven sensor drift during surveys. Incorporating calibration enhances inter-frequency correlations, reducing misfit in inverted data and improving trust in outcomes e.g., of sea ice surveys (Hunkeler et al., 2015) and surveys of other geophysical targets (Minsley et al., 2012; Brodie and Sambridge, 2006). For calibration of a commonly used commercial instrument, the GEM-2, Hunkeler et al. (2016b) rely on a site of known consolidated ice and snow thickness where the instrument is elevated step-wise above ground. Calibration parameters (gain factor, phase, Inphase, and Quadrature offset terms) are iteratively determined to minimize differences between observed and model-predicted responses. This is challenging in Atka Bay due to the ubiquitous presence of a SIPL with unknown conductivity. We propose an alternative efficient and simple approach to calibration leveraging the zero-conductivity environment on the ice shelf.

We also recognized the importance of investigating the impact of sledge motion, due to roughness of the snow surface formed by snow drifts, on the EM response and in turn the impact on the inverted parameters. Sledge motions observed qualitatively for towing instruments with snowmobile are significant. Signal distortions from pitch and roll of the sledge during surveying stem from changes in transmitter-receiver coil orientation, whenever the coils are not in an HCP orientation. For a roll angle of 90°, the recorded signal must be the well known response from a vertical-coplanar (VCP) coil orientation, and for roll angles between 0° and 90°, the signal must smoothly vary between HCP and VCP response (Guillemoteau et al., 2015; Yin and Fraser, 2004). Yin and Fraser (2004) derive equations for the HCP coil array under roll rotation assuming negligible coil separation relative to altitude, a condition typically met in airborne surveys in which the roll correction depends only on the HCP response and roll angle, where the response combines the initial HCP response with a cosine term and a constant factor. Numerical investigations into the impact of coil orientation changes on the recorded EM response have predominantly centered on aerial EM surveys (Yin and Fraser, 2004; Fitterman and Yin, 2004; Holladay et al., 1997) and shipborne EM measurements of Antarctic sea-ice thickness (Reid et al., 2003). Generally, changes in coil orientation that are typically encountered in airborne surveys are considered to have negligible effects. Computations for airborne geometries have demonstrated that pitch or roll angles of ±10° result in a maximum error of 1.5 % in the measured EM response for a horizontal-coplanar coil configuration (Holladay et al., 1997). Reid et al. (2003) report that for an EM31 at a 6 m altitude above a conductive half-space with 2500 mS/m, in a vertical-coplanar coil orientation, a 10° roll produces positive errors of 2.7 % in the inphase component and 2.3 % in the quadrature component. We will assess how these findings apply to our setup.

This paper presents operational improvements to the calibration method, inversion procedure of EM surveys and a detailed map of platelet ice thickness in Atka Bay. The established long term monitoring program on Atka Bay as part of the Antarctic Fast Ice Network (AFIN) (Arndt et al., 2020) together with the proven feasibility and potential of multi-frequency EM have led to a dedicated surveying effort in summer 2022/23 with 1000 km of EM surveys collected from October to January. The new calibration method together with inversion in a flexible computational environment was implemented to retrieve combined snow and ice, and SIPL layer thicknesses, as well as their conductivities with a high horizontal resolution of the inferred sea ice and SIPL properties. Our approach is supported by an EM forward model and an analysis of the impact of instrument and motion noise, and the results are validated by coincident manual drill-hole measurements. Our resulting SIPL maps cover the entire bay with an area of 325 km^2 and thus all potential ISW outflow zones. The dataset and processing is suitable to reveal temporal transitions of SIPL growth and decay in the future to attribute areas of different thickness to different oceanic conditions.

2. Methods and measurements

2.1. EM instrumentation and surveys

We utilize a commercially available multi-frequency EM induction instrument (GEM-2, Geophex Ltd.) with a transmitter-receiver coil spacing of 1.66 m and an additional bucking coil at 1.045 m from the transmitter. The instrument's design is suitable for low conductivity environments, compensating for the transmitter field using a bucking coil, under the assumption of a linear sensitivity of the bucking coil to the conductive subsurface. However, this compensation breaks down in highly conductive sea ice surroundings, resulting in a bucking-coil bias (Hunkeler et al., 2016a). To address this issue, we apply the bias correction scheme from Hunkeler et al. (2016a) by accounting for the bucking coil as a second effective receiver coil in our calculations.

The instrument setup includes frequencies of 1530, 5310, 18,330, 63,030, and 93,090 Hz with a sampling rate of 10 Hz, consistent with measurements from 2015 (Hunkeler et al., 2016b). The GEM-2 response includes Inphase and Quadrature signals at each frequency in parts per million. The instrument was mounted in a sled, 20 cm above the snow, and towed behind a snowmobile using an 8 m long rope, allowing for survey speeds between 10 and 30 km/h, depending on surface conditions. At these speeds, the sled may roll by angles of up to 30° due to roughness from snow drifts, impacting the EM signal.

A GPS antenna (GARMIN GPSx LVC, 5 m,) connected to the GEM-2 provides positions with 3–15 m accuracy for each EM measurement (Garmin Ltd, 2024). The data has been rigorously checked for spatial consistency. Consecutive measurement points align smoothly along the intended tracks, with no significant deviations observed. Furthermore, over 80 % of the data points were obtained with WAAS (Wide Area Augmentation System) fixes, which provide an accuracy better than 3 m (Garmin Ltd, 2024).

Data for this study were collected on the seasonal first-year fast-ice in Atka Bay between 27 October 2022 and 3 January 2023. The dataset includes 24 coincident electromagnetic (EM) induction sounding surveys conducted along grid lines across the entire bay, totaling approximately 1000 km of EM and GPS data (Fig. 1B).

2.2. Manual thickness drilling

Manual drill holes are used to validate the retrieved thicknesses from the EM method. Sea ice thickness, snow depth and freeboard are measured with regular thickness tapes. SIPL thickness is determined using the metal-bar method (Crocker, 1988), which is subject to a potential underestimation of the SIPL thickness of up to 30 cm, due to the uncompacted interface at the ocean-platelet ice boundary and the

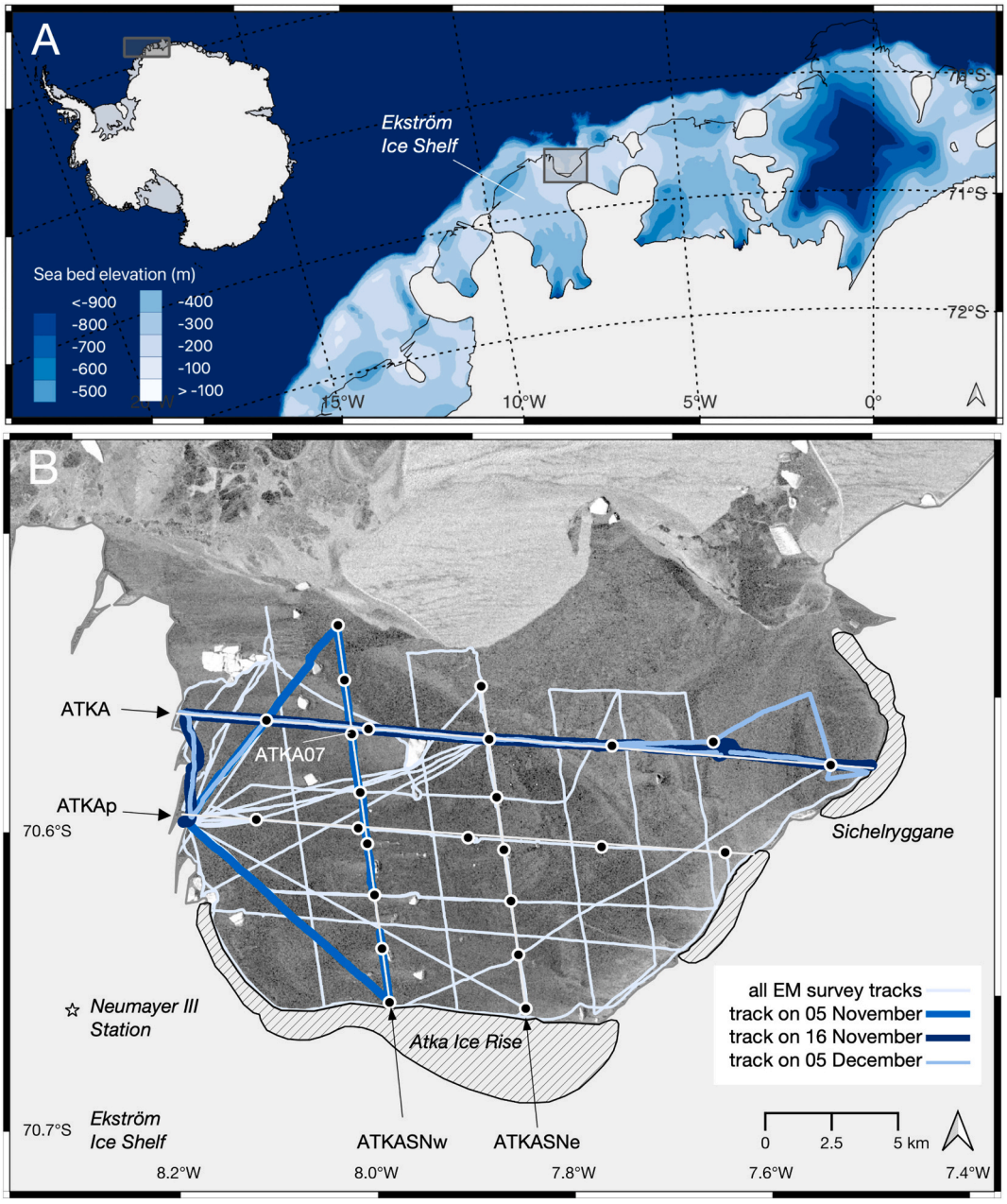

Fig. 1. A) Location of Atka Bay in Dronning Maud Land, Antarctica. Ice sheets are depicted in white, and ice shelves are transparent. The colormap illustrates the seafloor topography based on the International Bathymetric Chart of the Southern Ocean (IBCSO v2) (Dorschel et al., 2022). The inset map of Antarctica shows land and ice sheets in off-white, with ice shelves in grey. B) Detailed map of Atka Bay, including the Ekström Ice Shelf and Neumayer III Station. White lines mark the four drill hole transects (ATKA, ATKAp, ATKASNw, and ATKASNe) during the 2022/23 summer season. The ATKA transect is the long-term monitoring transect conducted as part of the AFIN program. Black circles indicate drill hole locations along the transects, while white lines represent all EM survey tracks. EM tracks of particular relevance later in this paper are shown in varying shades of blue. The background is a TerraSAR-X image from 9 November 2022, courtesy of the German Aerospace Center (DLR). Hashed areas denote where the ice shelf is grounded. Both maps are in Antarctic Polar Stereographic projection (EPSG:3031). (For interpretation of the references to colour in this figure legend, the reader is referred to the web version of this article.)

partial destruction, and thus compression, of platelet crystals upon impact of the metal bar (Hoppmann et al., 2015b).

Four manual drilling transects, two of which were repeated, were conducted between October and December 2022, with simultaneous co-located GEM-2 surveys at the locations shown in Fig. 1B. At each site, five drill holes were strategically positioned approximately 5 m apart to account for small-scale spatial variability. Due to time and logistical constraints during our fieldwork, we occasionally reduced the number of drill holes from five to three at certain sites. The average thicknesses for each transect are detailed in Table B1.

2.3. Calibration and sensor drift correction

Retrieving precise layer thicknesses and conductivities necessitates the consideration and correction of system calibration offsets and drift. The calibration and determination of drift involves placing the instrument in a zero-conductivity environment — on top of the ice shelf — for a defined period both before and after each sea ice survey. The instrument is left undisturbed in this environment and the EM repsonse is recorded for at least 10 s before the start of each survey and after completing the survey on sea ice. The minimum duration is deemed sufficient for the system to stabilize and to capture instrumental noise. Beyond that minimum duration, no standardized protocol exists for the operator, resulting in varying recording times that range from 32 to 800 s (mean: 197 s) before the survey and from 12 to 200 s (mean: 60 s) after the survey. The calibration and drift correction time intervals were manually selected based on a visual inspection of the data.

During the calibration period, we record the instrument's Inphase and Quadrature responses at each operating frequency, measuring the so-called free air offsets. The mean value of these offsets is calculated for each frequency, and the resulting offsets are then subtracted from the survey data to correct for any baseline shift.

Regarding the calibration for gain and phase, no additional steps were taken in this study. Unlike previous work, such as Hunkeler et al. (2015), where a known subsurface conductivity environment was available for repeated height-step ladder calibrations to account for gain and phase, Atka Bay, due to the presence of a platelet layer across the entire area in late winter, does not provide an environment with a known subsurface of non-zero conductivity. As a result, we relied solely on the zero-conductivity calibration and did not perform a calibration for gain and phase shifts. In this study, we demonstrate that for measuring SIPL thickness and conductivity, the free-air offset calibration, combined with drift correction during each survey, proves to be sufficiently accurate.

Drift correction is necessary to account for potential gradual changes in the instrument's baseline response over the survey duration, although the magnitude of the drift is not known a priori and may be insignificant. Drift is monitored by performing the repeated "free-air" measurements over the ice shelf immediately following each transect. A linear drift correction model is applied by interpolating between the initial calibration before the transect and the post-transect calibration, assuming that any drift follows a linear trend during the survey. Fig. 2B illustrates the measured signal before and after the application of both calibration and drift correction.

To assess the robustness of our calibration and drift correction procedures, we analyze the temporal variability in the free-air offsets and drift across all surveys. Table 1 provides the mean offsets and their standard deviations, calculated over all surveys. This analysis allows us to quantify the variability of the offsets and demonstrate their significance relative to the final calibrated and drift-corrected signal. To contextualize these offsets, we express them as a percentage of the average signal measured on sea ice during a representative survey along the ATKA standard line on 16 November 2022.

Before the inversion process, the EM data are re-sampled to a 1-m along-track point spacing by taking the nearest EM data point and linearly interpolating between adjacent GPS measurements.

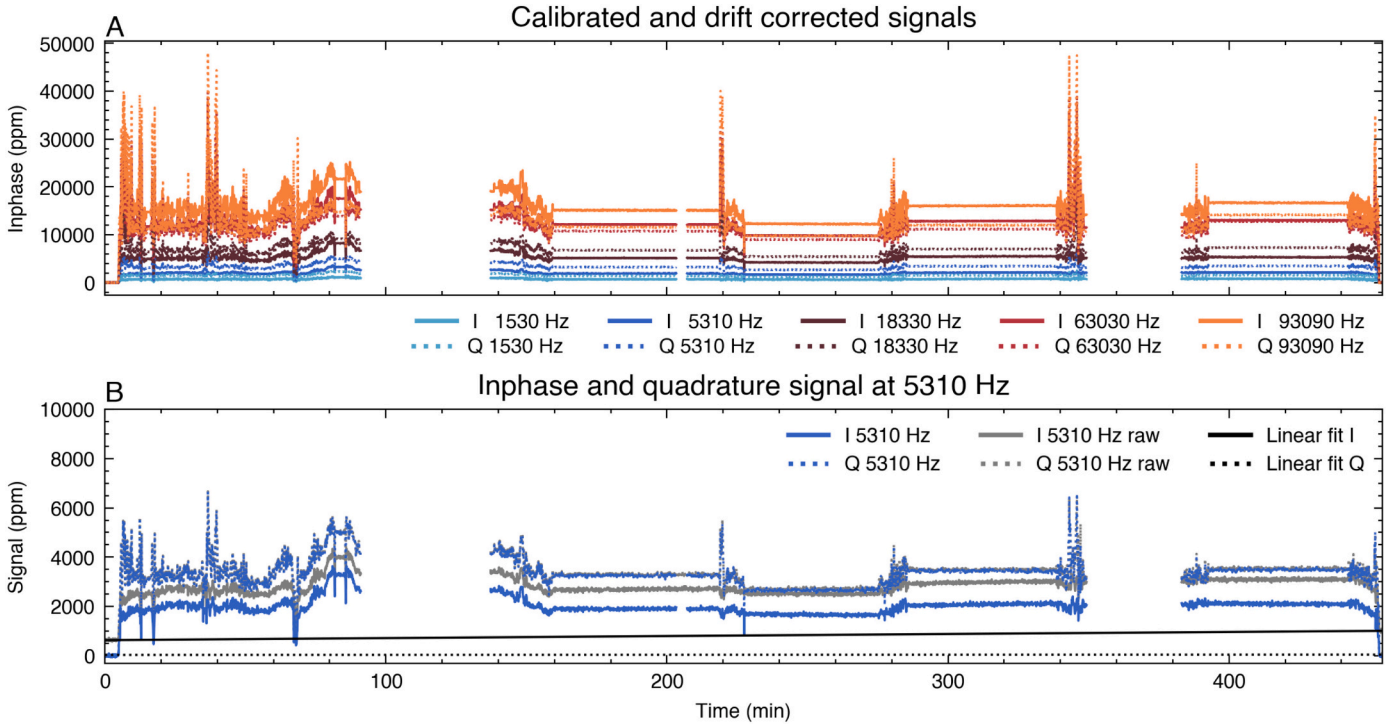

Fig. 2. A: EM measurements along the transect of 05 December 2022, with raw data for the Inphase and Quadrature signals. The grey lines are raw data before calibration. B: Inphase and Quadrature signal at 5310 Hz before (solid and stippled grey lines) and after (blue solid and stippled lines) calibration and drift correction. The linear fits (solid and stippled black lines) are used for drift correction. The time periods where the signal is relatively constant are the intervals where the GEM-2 was not moving while manual drilling was conducted and show the instrument noise. (For interpretation of the references to colour in this figure legend, the reader is referred to the web version of this article.)

Table 1
Mean±standard deviation of Inphase (I) or Quadrature (Q) response at the respective frequency during calibration and drift correction in a zero-conductivity environment, i.e., in free-space on the ice shelf. Refer to Fig. 2 for an illustration of the calibration and drift correction procedure. The computed values represent the overall mean across all transects. Additionally, the mean±standard deviation is reported in % relative to respective mean signal during a representative survey on sea ice (ATKA standard line on 16 November 2022).

I or Q	Frequency (Hz)	Offset (ppm)	Offset/mean signal (%)	Drift (ppm)	Drift/mean signal (%)
I	1530	1307±144	145±16	116±162	13±18
Q	1530	521±67	33±4	3±73	0±5
I	5310	763±166	34±7	126±201	6±9
Q	5310	78±72	2±2	4±88	0±2
I	18,330	863±198	15±4	126±228	2±4
Q	18,330	592±77	8±1	−3±64	0±1
I	63,030	0±247	0±2	128±273	1±2
Q	63,030	305±106	2±1	−107±47	−1±0
I	93,090	−828±340	−5±2	168±333	1±2
Q	93,090	−2618±387	−19±3	−437±164	−3±1

2.4. Noise

We distinguish between two sources of noise: Random instrument noise, that would also occur if the instrument is at rest, and motion noise resulting from tilt and roll of the sled (motion noise).

The random noise is assessed as the signal's standard deviation with the instrument at rest, once in a free space environment (during calibration on the ice shelf) and on the sea ice during a typical transect (Table 2). The different environments are chosen to assess whether the random noise level is independent of the signal strength.

We assess whether the minimal influence of motion noise observed in previous studies is applicable to our specific case. This assessment is based on assumptions drawn from the observed sled motion during the survey process, where notable rolling motion of the sled is observed, while pitch remains negligible over level ice. We model the response of tilted dipole transmitters and receivers using the software empymod (Werthmüller, 2017) with a subsurface model that is representative of the mean conditions in Atka Bay (2.5 m thick ice+snow, and 4.9 m thick SIPL with conductivities of 20 mS/m for ice+snow, 830 mS/m for platelet ice and 2700 mS/m for seawater). Modeling the percentage error for roll angles up to 90° results in cosine curves with the maximum error at 90° angles as shown in Fig. 3A. The maximum percentage error is −45 to −50 % for the Inphase signals. The Quadrature components have smaller maximum errors of −25 to −45 %.

The percentage error in the Quadrature components is significantly affected by the modeled conductivity of the ice+snow layer. When varying the conductivity of the ice and snow layer from 0 to 50 mS/m, a reasonable range, the Quadrature errors shift from −43 to −48 % at zero conductivity, decreasing in magnitude to −9 to −41 % as conductivity increases to 50 mS/m. Therefore, we focused our analysis on the modeled cosine curve illustrated in Fig. 3A, recognizing that this approach may overestimate noise, particularly in the Quadrature components for large roll angles.

We make the assumption that roll angles during surveying conform to a Gaussian distribution with a mean of zero and standard deviation of 13°. This estimate is based on field observations, where extreme roll angles of approximately 50° were occasionally observed, corresponding to about three standard deviations. In the absence of pitch and roll measurements, this value serves as a reasonable approximation, though actual roll angles may vary due to factors such as surface roughness and driving speed.

With this assumption, we can introduce a noise component to the EM response attributed to roll, by applying the modeled instrument roll noise to a constant 5310 Hz Inphase signal. We found the resulting signal probability density distribution to be best described by a Gamma distribution. Fig. 3B shows an exemplary probability density distribution of the EM response, in this case for the Inphase signal at 5310 Hz. The rolling motion introduces a negative bias in the signal's mean value. Alongside the histogram of 1000 measurements with artificial motion noise we show the histogram of 1000 actual measurements with a stationary instrument (station ATKA07, transect on 16 Nov 2022), where the variations represent instrument noise. In both histograms, the one-sided widths are similar, indicating that motion noise and instrument noise have a comparable level of influence.

In our case, the error introduced by coil orientation is coherent across frequencies and is expected to smoothly vary between subsequent data points, as the sampling rate at 10 Hz is higher than the frequency with which the sled typically rolls. This coherent error cannot be removed by filtering techniques for random noise, see for example (Martinelli and Duplaá, 2008; Minsley et al., 2012). In the results section, we illustrate the impact of the two noise types on the inverted properties, shown in Fig. 3, C—F, and the expected percentage root-mean square error (%RMSE), with

$$\%RMSE = \frac{\sqrt{\frac{1}{N}\sum_{i=1}^{N}\left(d_{\mathrm{meas},i} - d_{\mathrm{calc},i}\right)^2}}{\overline{d_{\mathrm{meas}}}} \cdot 100 \quad (1)$$

where $d_{\mathrm{meas},i}$ are the measured I and Q responses at each frequency and $d_{\mathrm{calc},i}$ are the I and Q responses calculated for the forward model of the subsurface resulting from the inversion and N is the number of measurements, 10 in our case.

Table 2
Instrument noise averaged for all calibrations on the ice shelf and during all station times (GEM-2 at rest) on transect along ATKA standard on 16 Nov.

I or Q	Frequency (Hz)	Mean noise, calibration (ppm)	Mean noise, station time (ppm)	Mean noise, % of the signal, station time
I	1530	46	45	5.4
Q	1530	43	42	2.1
I	5310	40	43	0.9
Q	5310	39	48	0.4
I	18,330	40	66	0.5
Q	18,330	40	44	3.2
I	63,030	45	40	1.3
Q	63,030	44	40	0.6
I	93,090	61	52	0.5
Q	93,090	62	77	0.6

2.5. Geophysical inversion

For the forward model we define three separate subsurface layers: The topmost layer is the consolidated sea ice plus snow (hereafter ice+snow layer), below is the SIPL. The lowest layer, modeled with infinite thickness, is the seawater. Although the snow cover usually exhibits a much lower electrical conductivity close to 0 mS/m (or much higher in case of surface flooding) than sea ice with 0–50 mS/m (Haas et al., 1997), sea ice and snow are commonly treated as one layer because they are indistinguishable by EM induction (Hunkeler et al., 2015, 2016b; Brett et al., 2020; Haas et al., 2021).

For inversion of the EM response of a horizontal-coplanar instrument to a horizontally isotropic layered medium we use the Python EMagPy API framework (McLachlan et al., 2021). We modified the forward model to account for the bucking coil bias, implementing the bucking coil as a second receiver according to Hunkeler et al. (2016a). To find a fast and reliable algorithm, we inverted synthetic data for a range of free parameters in combination with different starting models (initial assumption of the values for free parameters). Refer to Supplement 2 for

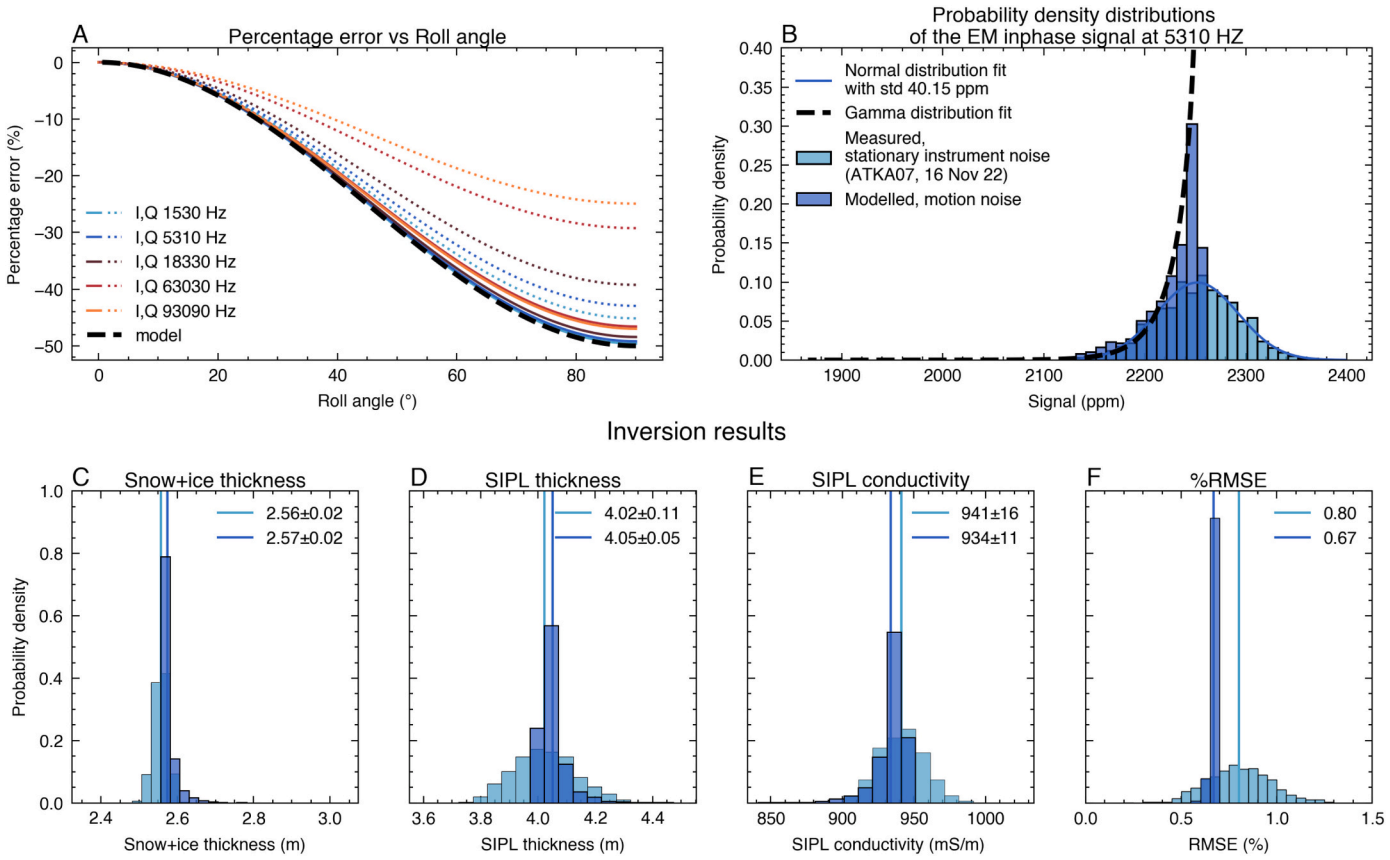

Fig. 3. A: Percentage error for the Inphase and Quadrature responses at the different frequencies depending on roll angle. The dashed black curve illustrates the model that we use to calculate the percentage error at a given roll angle (the same for all frequencies). B: Probability density distributions for the Inphase EM response at 5310 Hz. The respnse from the stationary instrument as measured at station ATKA07, during the transect on 16 November 2022 (light blue) is shown alongside the modeled motion noise with our assumptions regarding the rolling motion during surveys (dark blue). The actual noise expected during the surveys represents the combined contributions from both noise sources. The fitted probability density distributions are also shown. C-E: Histograms of inverted properties for an EM response with noise characteristics as shown in panel B. Legend states mean±1std. F: Histogram of the %RMSE between measured EM response and forward model EM response to a subsurface with the inverted parameters. Legend states mean %RMSE. (For interpretation of the references to colour in this figure legend, the reader is referred to the web version of this article.)

a detailed description of EMagPy features, algorithm and starting model selection, and the performance of the selected Sequential Least Squares Programming (SLSQP) algorithm. Hunkeler et al. (2016b) showed by non-linear most-squares inversion that model parameters are constrained well by the data using the same instrument configuration, forward model, and expected range for the free parameters as in this study.

In all inversions of field data, the starting model is set to an ice+snow layer thickness of 2.5 m and conductivity of 0 mS/m, a SIPL layer thickness of 2.5 m and conductivity of 600 mS/m, and a homogeneous half space with conductivity of 2700 mS/m for seawater. The allowed ranges for ice+snow and SIPL thicknesses are both set to 0.5–15 m. The allowed range for ice+snow conductivity is 0–200 mS/m, and the range for SIPL conductivity 400–1800 mS/m. The selection of the initial model and the ranges is determined through a comparison of various starting models presented in Supplement 2, along with the thickness data obtained from drill holes. The seawater conductivity of 2700 mS/m was assumed to be constant and is well known from CTD measurements.

2.6. Post-processing of inversion results: filtering

As the fast ice is rather level and uniform, we use a lateral constraint filter to exclude inversion results with implausible layer properties. Results that deviated in layer thickness by more than 2 m (ice+snow) and by more than 2 m (SIPL) from any thickness within a distance of 20 m were excluded. Results that reached the boundary conditions for the free parameters were also excluded. To check the validity of our inversion and filtering, we calculate the percentage root-mean-square-error (%RMSE) before and after filtering for each transect according to Eq. 1. The %RMSE for each inverted data point on the transect is expected not to exceed the average %RMSE created by random instrument noise, if the inversion was successful. Fig. 3F shows the %RMSE for a typical signal with random noise, where the mean %RMSE is 0.8. Following the approach outlined by Hunkeler et al. (2016b), we excluded stations with an RMSE >10 from all further calculations. This threshold was determined based on a visual inspection of the inversion results, allowing us to omit outliers and implausible values.

2.7. Validation with manual drill holes

To validate the inversion results, we utilized six drill holes located along the transect lines specified in Table B1. These holes were drilled simultaneously or within one day of the corresponding EM measurement. Because of time limitations, we were unable to stop and annotate sections of EM data that coincided with the drill holes. Instead, we simply passed over the drill hole locations without stopping, and co-location was conducted post-survey using the recorded GPS data from both the drill holes and EM surveys. All EM-thicknesses within 20 m of the respective drill hole site were averaged to a mean value and drilled thicknesses were also averaged per site. The standard deviation of the mean EM thickness was used to perform a weighted linear regression of EM thicknesses vs drilled thicknesses. Further, we compute the RMSE between observed and predicted EM thicknesses. Gathering all EM Data

within a 20 m radius was necessary given the limited GPS precision when choosing the manual drill hole sites and the limited precision of the GEM-2 GPS.

3. Results

3.1. Calibration and drift correction

The mean signal offsets from zero of the 26 calibrations range from −19 % to +145 % of the respective mean signal at the different frequencies during a representative survey on sea ice (Table 1). The Quadrature signal at 18330 Hz exhibits the lowest temporal variability, with 1 % of the mean signal strength. The Inphase signal at 1530 Hz exhibits the highest temporal variability, with 16 % of the mean signal strength. For almost all frequencies, the temporal variability (67–387 ppm) is larger than the instrument random noise (39–77 ppm, Table 2), thus pre- and post-survey calibration for each transect will significantly improve the accuracy of the inversion.

The mean signal drift ranges between −3 % to +2 % for most frequencies, except for the Inphase signals at 1530 and 5310 Hz, which exhibit a higher mean drift of 13 % and 6 %, respectively. The variability of drift behaviour is within the same order of magnitude as the mean drift, and thus again significant compared to the instrument's random noise.

3.2. Noise

Instrument noise is not influenced by subsurface conductivity, and noise levels are similar across all frequencies with a range of 40–77 ppm, representing 0.4 % to 5.4 % of a typical signal over sea ice. Instrument noise levels on the sea ice are consistent with levels observed during calibrations in low-conductivity environments. Table 2 provides information on instrument noise and the percentage noise relative to the signal at the corresponding frequency.

The influence of the roll motion is expected to contribute to the accuracy of the inversion results in the same order of magnitude as the random instrument noise. Fig. 3C-F shows the inverted parameter's distribution compared to that for a representative station (ATKA07, 16 Nov 2022). For influence of noise on the inverted properties at other stations on the same survey date, see Table B2. The bias introduced by the rolling motion adds only a few cm for both layer thicknesses; the introduced uncertainty is in the same order as for the random noise: ±2–8 cm for the ice+snow thickness, and ±6–13 cm for the SIPL thickness. The SIPL conductivity bias from rolling motion is about −10 mS/m and the uncertainty of ±16–22 mS/m is again similar to that created by random noise. The mean %RMSE for both noise types is about 0.8.

3.3. Inversion results and filtering

Overall, the inversion procedure, coupled with the filtering, yields reliable results for both the consolidated ice+snow thickness, as well as the SIPL thickness. The mean %RMSE of all inverted surveys before filtering was 1.2, and thus only slightly larger than the mean %RMSE of 0.8 expected from instrument noise, indicating that the desired misfit was reached for most measurements. After applying filtering, excluded data were mostly from survey sections close to the ice shelf edge with very deep snow accumulations and over platelet ice that was thicker than 10 m, e.g. the first and last survey km in the transect shown in Fig. 4, indicating the sensitivity limits for very thick ice+snow and platelet layers. The existence of a very thick SIPL was validated by an opportunistic drill hole, not associated with ans GEM-2 survey, with a 14 m SIPL. Another frequently encountered exclusion criterion involved reaching the lower conductivity model threshold for the SIPL conductivity (400 ppm). After filtering, on average 80 % of the data from each transect were retained. For specific details on the filtering outcomes of individual transects, please refer to Table B3.

3.4. Validation with manual drill holes

Comparison of EM-derived thicknesses with drilled thicknesses shows that the EM results for the layer thicknesses are within uncertainty and in very good agreement with drill hole measurements (Fig. 5). Ice+snow thickness is underestimated with the EM method by 0.05 m on average. The mean SIPL thickness difference between the methods is 0.17 m. The RMSE between measured EM thickness and predicted EM thickness from the weighted linear regression is 0.39 m.

3.5. Sea ice and SIPL maps

We computed maps of interpolated and gridded EM inversion results for the SIPL thickness (Fig. 6B) and SIPL conductivity (Fig. 7A) for all surveys between 3 December and 17 December. Within this timeframe we assumed that the SIPL thickness has changed little to be comparable at intersecting survey lines. Spatial interpolation of EM SIPL thickness and conductivity to a 100 m horizontal resolution grid was accomplished through ordinary kriging. Survey transect spacing in the bay was 2.2 km at maximum, with closer spacing between adjacent transects in

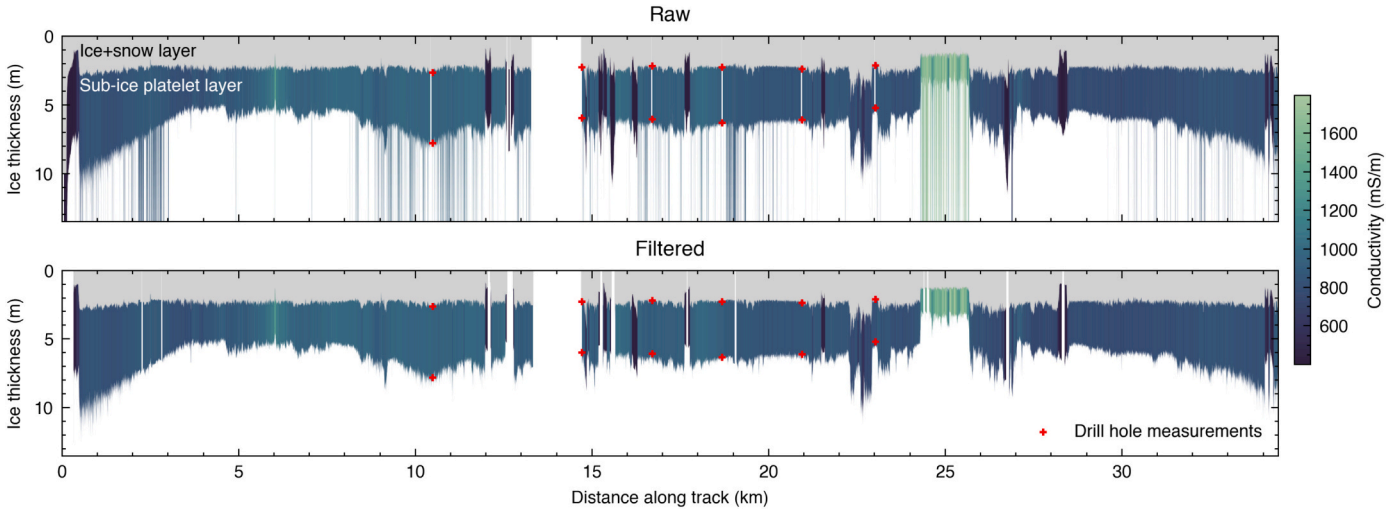

Fig. 4. Inverted (top) and inverted and filtered data (bottom) for the transect of 05 November. Red crosses indicate the mean snow+ice and SIPL thickness from co-located drill holes along the transect. (For interpretation of the references to colour in this figure legend, the reader is referred to the web version of this article.)

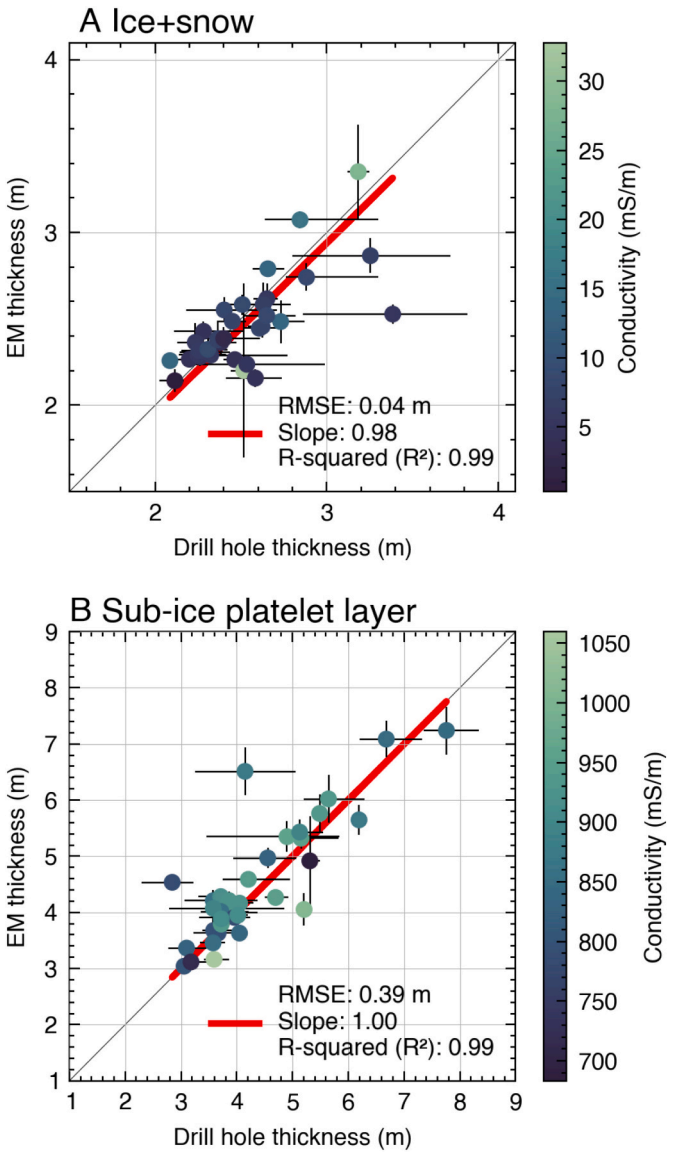

Fig. 5. Scatter plot of EM-derived thickness vs. drill hole thicknesses for A) the ice+snow layer and B) the SIPL, with symbol colour denoting conductivity. X-error is the minimum and maximum drill hole thickness, y-error is 1 standard deviation of the EM data. The black line is 1 vs 1.

most locations (Fig. 1).

For the consolidated ice and snow layer, no spatial interpolation was conducted (Fig. 6A). Across the bay, the thickness of consolidated ice+snow generally varies very little between 2 and 2.5 m, except around icebergs where EM thickness can reach up to 6.8 m in snow drifts on the windward side. In 2022, the fast-ice in Atka Bay formed between 2 April to 12 May, progressing from the west to the east, accompanied by rearrangements and rafting in that period. Notably, the very eastern bay remained open for a slightly extended duration but eventually froze on 20 May. A complete freeze-up of the bay by the end of April is considered typical (Arndt et al., 2020). Consequently, the modal EM ice+snow thickness of 2.4 m corresponds to the typical thickness of thermodynamically grown first-year sea ice with a snow cover in Atka Bay, as reported by Arndt et al. (2020). Further, the modal EM ice+snow thickness agrees with the mean drill hole ice thickness for the north-south and the east-west transect in December 2022, with mean thicknesses of 2.34±0.56 m and 2.10±0.12 m for the consolidated ice, with 0.48±0.39 m and 0.61±0.34 m of snow, respectively (Table B1).

A region of the south-western bay, close to the ice shelf, with thick snow cover from preferential wind-driven accumulation in this area, exhibits EM derived ice+snow thicknesses below the expected 2 m, down to 0.72 m. This potentially indicates that snow accumulation causes flooding of the ice surface with seawater, leading to an increase of true electrical conductivities from the three-layer subsurface model. Unfortunately no drilling was conducted in this region to verify this effect.

The spatial distribution of SIPL displays distinct areas of varying thickness. The thickest SIPL was identified in the southeast near the ice-shelf edge, measuring 8–9 m (Fig. 6B). Similarly, larger thicknesses are also noticeable along the ice shelf edges on the western side of the bay, but are absent on the eastern side. A region of a relatively thin SIPL, with 2.5–3.0 m thickness, extends from north to south in the western part of the bay. Another area of lower thickness is located in the easternmost corner of the bay, where the SIPL measures 2.0–2.5 m thick. Notably, this area coincided with the region that froze last around 20 May.

The mean thickness of 4.9 m of all measurements is comparable to the average thickness of 5.3 m found by Hunkeler et al. (2016b) from several transects, mostly on the western bay in December 2012, but higher than the seasonal SIPL average annual maximum thickness of 3.91 m reported by Arndt et al. (2020) for drill holes on the main transect between 2010 and 2018, owing to the different regional coverage.

3.6. Platelet-layer conductivity and solid fraction

The inverted SIPL conductivity spans the entire permissible range from 400 to 1800 mS/m with a mean of of 830±127 mS/m. Post spatial interpolation, the highest conductivity values were observed in the easternmost bay (Fig. 7A), whereas low conductivity areas were identified at the western shelf edge and around larger icebergs. However, caution is warranted in interpreting these areas, as they likely indicate methodological limits due to elevated ice+snow thickness (up to 6 m) in the same regions. No discernible correlations between SIPL thickness and SIPL conductivity were observed.

For estimation of SIPL solid fraction β from the inverted electrical conductivities of the SIPL σ_{SIPL}, Archie's law is commonly used (Brett et al., 2020; Haas et al., 2021; Hoppmann et al., 2015b; Hunkeler et al., 2015, 2016b):

$$\beta = 1 - \sqrt[m]{\frac{\sigma_{brine}}{\sigma_{SIPL}}} \tag{2}$$

where σ_{brine} is the brine conductivity, which is assumed to correspond to the seawater conductivity (2700 mS/m), and m is the empirical cementation factor, which is not well known for the SIPL geometry.

In this study, the experimental cementation factor in Archie's law (Eq. 2) is derived from assessments of the SIPL's freeboard contribution at drill hole sites. We initially employ Archimedes' principle to estimate solid fractions using freeboard data from drilled holes. We limit our analysis to drill holes with positive ice freeboard ($\geq$ 2 cm) between October and January to avoid flooded sites. We calculate a theoretical ice freeboard for a seawater density of 1027.8 kg/m^3 at a salinity of 34.5 g/kg, first-year sea ice density of 920±10 kg/m^3 (Timco and Weeks, 2010), and snow density of 380±37 kg/m^3 (mean±std. for snow density measurements on Atka Bay in August 2011, (Hoppmann et al., 2012), and a platelet crystal density of freshwater ice (917 kg/m^3). We assigned an estimated uncertainty to sea ice and snow densities only, as these uncertainties are significantly larger than for the other densities. Further assigning a measurement uncertainty for a single measurement of ±2 cm for ice freeboard and snow depth measurements, the measured freeboard is 7.6±2.4 cm higher than the calculated freeboard, which translates to an average of 71±22 cm of freshwater ice estimated to cause the observed increase in freeboard. This calculation, based on the average SIPL thickness of 446 cm in the utilized drill holes (ignoring the uncertainties introduced by the potential underestimation with the

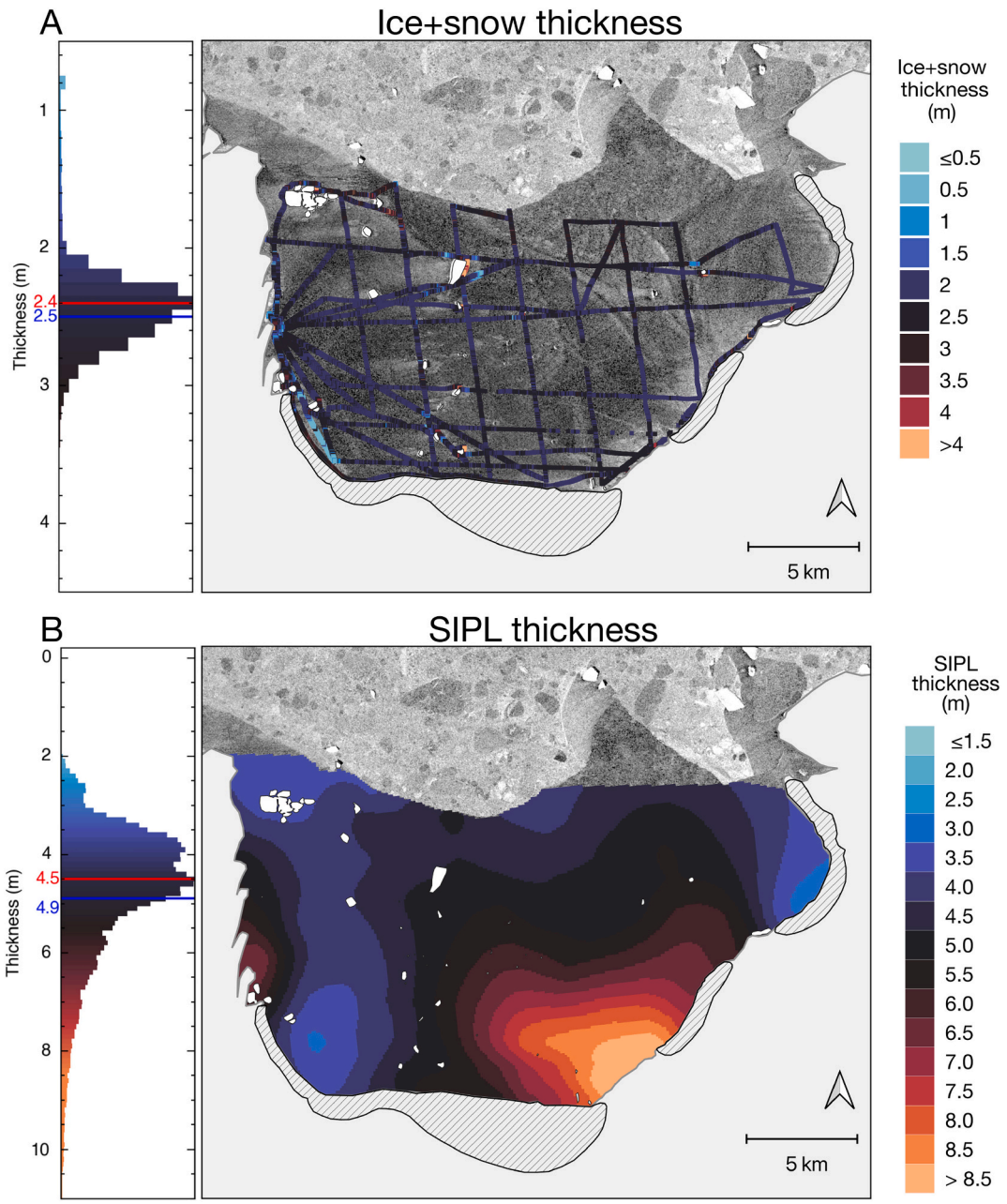

Fig. 6. Maps of EM-derived A) ice+snow layer thickness and B) EM-derived SIPL thickness. Left column shows the respective probability distribution, where the red line indicates the modal value, and the blue line indicates the mean value. Background images are TerraSAR-X images from 12 December 2022. (For interpretation of the references to colour in this figure legend, the reader is referred to the web version of this article.)

metal bar method), yields a solid fraction of 0.16±0.05. The average SIPL conductivity of GEM-2 surveys co-located with the drill holes is 870 mS/m. To achieve a mean EM solid fraction close to the upper estimate of the freeboard-derived solid fraction of 0.16 + 0.05, a cementation factor of about 5 is needed. Using this cementation factor, we obtained an average solid fraction of 0.22, with minimum and maximum solid fractions of 0.11 and 0.28, respectively (Fig. 7B).

4. Discussion

4.1. Limitations of the presented method

Despite careful calibration and selection of inversion methods, multi-frequency EM data still come with potential error sources. Hunkeler et al. (2016b) used absolute calibration coefficients derived from known ice thickness to correct Atka Bay transects. We employed calibration in a zero-conductivity environment on the ice shelf, accounting for offsets and drift in the EM signal. This calibration method is less time consuming compared to a height step calibration, where the instrument needs to be removed from its sledge and elevated step-wise on a ladder. The technique also accounts for GEM-2 positioning deviations and electronically induced instrument drift. Calibrations remain a prerequisite for accurate inversion results, as the offsets from zero in a non-conductive environment are large relative to the signal and vary significantly between survey dates, with no consistent trend over the whole field season. The instrument drift was variable between dates and frequencies and also warrants a correction.

Typical instrument noise and motion noise result in an uncertainty of

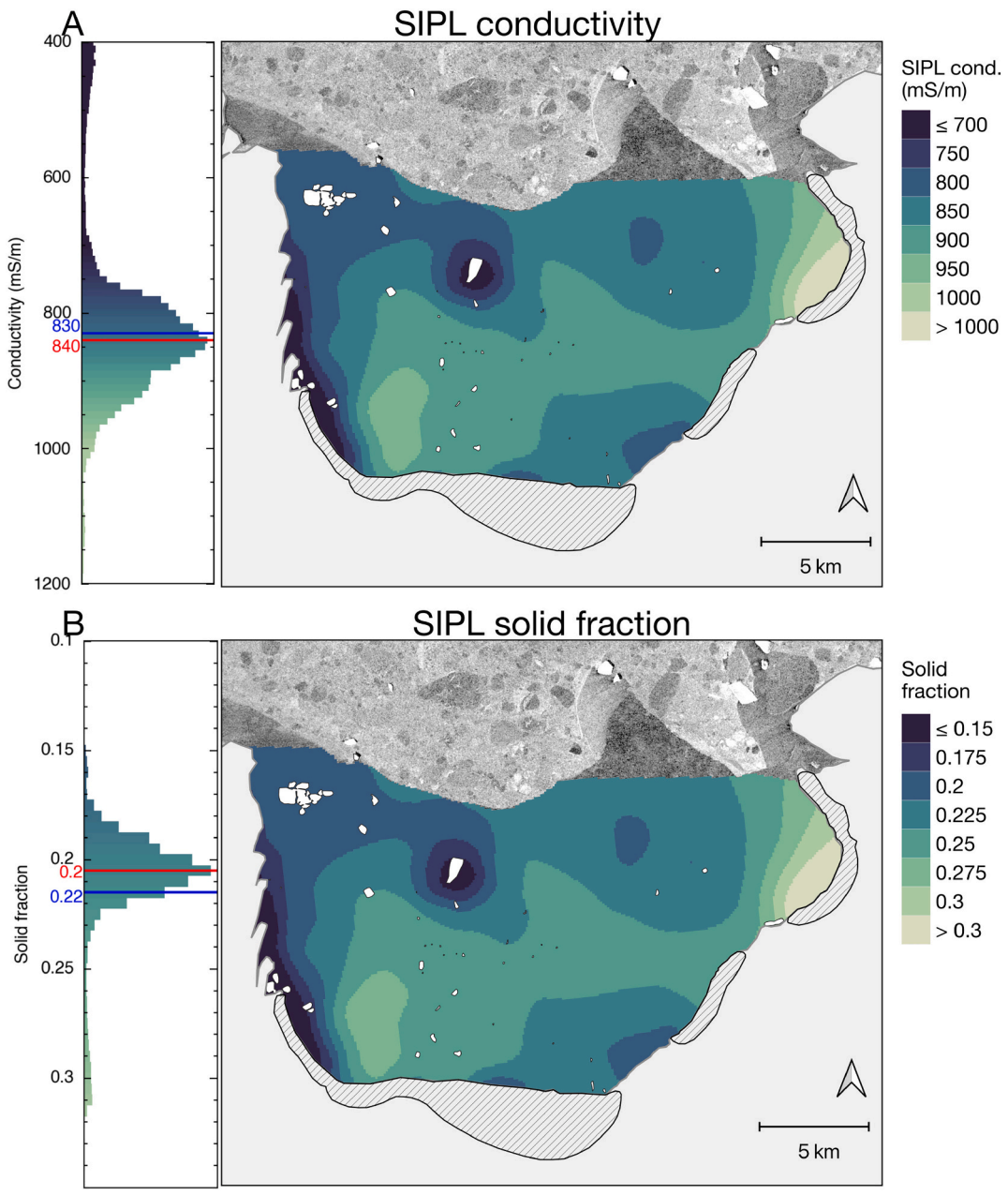

Fig. 7. Maps of A) SIPL conductivity and B) EM-derived SIPL solid fraction with respective probability distribution, where the red line indicates the modal value, and the blue line indicates the mean value. (For interpretation of the references to colour in this figure legend, the reader is referred to the web version of this article.)

inverted ice+snow thickness in the order of less than 5 cm and less than 15 cm for the SIPL, both contributing in a similar fashion. A more detailed analysis of motion-induced errors in the signal would only be possible with an inertial navigation system attached to the instrument's sledge. We conclude that at low survey speeds, the noise from instrument roll is only of secondary concern and does not prevent accurate inversion of layer thicknesses and SIPL conductivity. To accurately quantify and model the deviations induced by non-horizontal coil orientations, a motion sensor would be required in the future. Our noise model could be utilized to incorporate and correct for roll angles if they were known. This could be particularly valuable for advancing GEM-2 applications with uncrewed aerial vehicles (UAVs) in sea ice studies. In a study conducted over a low-conductivity test site using a GEM-2 towed 6 m below an UAV, Vilhelmsen and Døssing (2022) acknowledged the influence of roll, pitch, and heading on their measurements, indicating a correlation that is not simply linear (Fig. 3A). This non-linearity is expected to be more pronounced in a high-conductivity sea ice environment. Therefore, gaining insights into roll and pitch measurements can be crucial for future drone-borne applications, enhancing coverage and accessibility.

We validated a new, fast inversion algorithm for a large dataset with high spatial resolution. The inversion results undergo a filtering process based on criteria that guarantee an acceptable degree of lateral smoothness, while also rejecting results that extend beyond the boundary conditions of the free parameters. Since we did not apply any filtering before the inversion, the reduction of the %RMSE from 1.2 to 0.9 was considered a successful outcome of the filtering process.

Sensitivity checks on synthetic data revealed optimal outcomes with suitable starting models, indicating accurate inversion for layer thicknesses, meaning that the normalized differences between true and

inverted layer thicknesses are less than 10 % for the whole range of layer thicknesses between 1 and 5 m for sea ice+snow and 1 to 10 m for the SIPL. Sea ice conductivity for sea ice thickness less than 2 m and SIPL conductivity for SIPL thickness less than 2 m are not well represented (see Supplement 2), which is also relevant for and applicable to other fast ice regions.

Most of the field data in this study were collected over a 2–7 m thick SIPL, for which the thickness is well constrained (Hunkeler et al., 2016b). However, we must note that the southeastern region exhibited such a thick SIPL, with a maximum of 14 m from drilling, that it exceeds the sensitivity limits of the GEM-2. As a result, a larger proportion of data over thick platelet ice had to be excluded after inversion. It should be noted that drill hole measurements using the metal-bar method are prone to underestimating the true thickness by up to 0.3 m (Hoppmann et al., 2015a) and are subject to observer-biases. Despite this limitation, the agreement between the SIPL thickness and the drill-hole measurements was generally satisfactory.

The simplified 3-layer model focuses on platelet-layer thickness, the primary parameter of interest. The highest EM-derived ice+snow thickness of 6.8 m was caused by snow drifts up to 3 m high close to an iceberg. In these locations, surface flooding could have formed a highly conductive layer of slush on top of the sea ice. This is not accounted for by the 3-layer model, but can be observed through higher inverted ice+snow conductivities in areas where flooding was observed with drill holes, particularly around icebergs and at the western shelf edge where there are large snow drifts. The presence of slush led to an underestimation of the sea ice+snow thickness of up to 1.5 m, when compared to drill holes, with an uncertain influence on the retrieved SIPL thickness. Unfortunately, the absence of drill hole data of flooded ice hinders a quantitative assessment of the effect of flooding on the retrieved layer thicknesses. Including a slush layer with variable conductivity and thickness would require a five-layer model (snow, slush, ice, platelet ice, seawater). Subsequent studies could investigate whether the parameters of interest are adequately constrained within this expanded model, if more drill hole data were also available from the snow drifts.

The choice to represent the SIPL in a 3-layer model by one layer of a constant conductivity is based on nearly isothermal nature of the SIPL and vertical homogeneity in brine salinity, as confirmed by studies (Hoppmann et al., 2015b; Robinson et al., 2014; Wongpan et al., 2021). However, some qualitative field observations suggest potential vertical gradients in solid fraction and, consequently, conductivity. For instance, Brett et al. (2020) observed a less-dense layer near the base of the SIPL at some drill holes near McMurdo in 2017, and similar nonuniformities were noted in Atka Bay by Hoppmann et al. (2015b). While these findings indicate localized vertical variability, the magnitude of this effect remains unquantified due to the challenges in directly measuring SIPL porosity and conductivity. This suggests that the assumption of uniform SIPL conductivity may not fully capture vertical variations and could lead to over- or underestimation of SIPL thickness. Inversion of EM surveys incorporating a multi-layered SIPL structure would be valuable, but additional in-situ data is essential for validating and refining such models.

The use of a 1D approximation in the horizontal dimensions introduces some modeling uncertainty, as documented in previous sea ice electromagnetic induction sounding studies (e.g., Reid et al. (2003)). However, in our case, the ice surface was relatively level, and only a small fraction of the data was collected over pronounced deformation with dimensions of the deformations comparable to or smaller than the instrument footprint. As a result, we have chosen to neglect the errors associated with the 1D approximation. Furthermore, probabilistic schemes, such as the one suggested by Wu et al. (2023) and Zaru et al. (2024), offer the capability to naturally incorporate prior information into the model and directly asses model uncertainties and improving subsurface interpretations, particularly when combined with in-situ data on SIPL solid fraction and knowledge about potential vertical gradients of the solid fraction within the SIPL.

4.2. Implications for ice-ocean processes

Our study presents the first complete map of the SIPL in Atka Bay, offering new insights into the ice-ocean interaction in this region.

The electrical conductivity of the SIPL obtained through inversion (Fig. 7) provides insights into the relative compaction of the ice platelets. A thicker SIPL may undergo increased compaction due to greater buoyancy of underlying platelets and compaction and consolidation, resulting in lower conductivity. While we could not identify a clear correlation between thickness and conductivity in our dataset, a qualitative observation indicates that the thick SIPL in the west, likely the oldest due to an earlier freeze-up in late March, is less conductive compared to the relatively thin and potentially younger SIPL in the easternmost location, freezing up at the end of May, validating the general plausibility of the variations of conductivity.

Notably, our average conductivity of 830±127 mS/m in December 2022 is lower than the overall average of 1200±400 mS/m for all EM transects in December 2012 (Hunkeler et al., 2016b). One potential explanation for this difference could be the relatively large fraction of SIPL that accumulated only after an August break-up in Hunkeler's EM dataset. In contrast, our EM surveys in 2022 were conducted over SIPL that started to build up in mid-April, and potentially underwent more compaction since then. The inter-annual variability of mean SIPL is further supported by Haas et al. (2021), who documented variations in SIPL conductivity in McMurdo Sound. They reported values ranging from 900 to 1500 mS/m over three years with a thicker SIPL and 1000 to 1800 mS/m over two years with a thinner SIPL, using airborne single-frequency EM measurements calibrated against drill hole thicknesses.

For the relationship between SIPL thickness and conductivity, Hunkeler et al. (2016b) and Hoppmann et al. (2015b) found a negative correlation. This was linked to variations in conductivity across areas with different onset of SIPL formation. The onset periods exhibited greater variability within their season and were constrained by the earliest establishment of a solid sea ice cover in March in some areas, and by a late storm-related break up of other areas in October. Specifically, they observed that thicker ice tends to have lower conductivity, with older ice typically being thicker. In contrast, our dataset shows no correlation between SIPL thickness and conductivity. Given that our dataset covers a SIPL that started to form within the same month, we suggest that age may have a greater influence on conductivity reduction through consolidation than thickness alone. However, it is important to note that our dataset may not be robust enough to draw definitive conclusions. Further investigation, particularly focusing on the evolution from initial formation to winter, is needed to provide more conclusive answers to this question.

Solid fractions, calculated through electrical conductivity, depend on the empirical cementation factor, but assuming uniformity across all SIPL thickness regimes might be an oversimplification. The mean solid fractions derived from a cementation factor of $m = 5$ was 0.22. However, the use of a cementation factor of $m = 3$ (Hunkeler et al., 2016b) in Archie's law would lead to an implausibly high mean solid fraction of 0.33 that contradicts observations from freeboard differences in this study, as well as other studies on SIPL solid fraction. Consequently, it became evident that a higher cementation factor, such as 5, was indeed necessary to obtain reasonable solid fractions from our inverted conductivities.

The EM method yields solid fractions of 0.11–0.28 in this study, compared to 0.20–0.43 in Hunkeler et al. (2016a) and Hunkeler et al. (2016b). The conversion relies on an empirical cementation factor that

depends on the grain shape and the pore geometry in the SIPL. By adapting a simple structural model originally designed for sea ice pore microstructure by Jones et al. (2012) and applying it to airborne electromagnetic surveys of the SIPL, Haas et al. (2021) demonstrated a variation in solid fractions ranging from 0.09 to 0.47. The reported values in this study align with estimates from energy balance sea-ice temperature profiles (0.18, Hoppmann et al. (2015a)), with modeled ice growth fits to observations (0.18 and 0.26, Hoppmann et al. (2015a, 2015b)), and with simulations of solid fraction (0.22, Wongpan et al. (2015)). However, they are lower than the fractions obtained from volume measurements in a bucket sample retrieved from a crack in the fast-ice in the western bay close to the ice shelf (0.36–0.54, Günther and Dieckmann (1999)). This emphasizes the need for further in-situ observations of platelet crystal geometry and consolidation degree to distinguish between artifacts from various EM methods and genuine spatial and temporal variability.

In the examination of the basal melt volume of the Ekström Ice Shelf associated with the SIPL, the respective SIPL average thickness of 4 m and 5.3 m, implies 22 % and 27 % of the Ekström Ice Shelf's basal melt volume is stored in the SIPL, respectively (Hoppmann et al., 2015b; Hunkeler et al., 2016b). Our study found an average thickness of 4.9 m, implying an intermediate value between the two previous findings. Hoppmann et al. (2015b) and Hunkeler et al. (2016b) have identified the deep cavity of the western Ekström Ice Shelf, situated 60 to 125 km south of Atka Bay, as the source of ISW. This conclusion has been drawn from camera observations of frazil outflow at the western bay, indicting eastward advection, together with the assumption that the eastern cavity, due to its limited depth, is unlikely to contribute significantly to ISW supply (Hoppmann et al., 2015b). However, our investigation aims to challenge this understanding. Our study has identified the thickest SIPL adjacent to a potential outflow area of the eastern cavity, precisely where the shelf is ungrounded between the grounded regions of Atka Ice Rise and Sichelryggane. This observation prompts a reevaluation of the role of the eastern cavity in basal meltwater dynamics. It is noteworthy that previous SIPL distribution studies (Hoppmann et al., 2015b; Hunkeler et al., 2016b; Arndt et al., 2020) did not cover the southeastern area of the sea ice, which is contiguous with the eastern cavity of the Ekström Ice Shelf. This cavity remains poorly studied in terms of its mass balance and bathymetry, highlighting a gap in our current understanding.

Additionally, recent findings suggest that the cavity beneath the western Ekström Ice Shelf is deeper than previously thought, as indicated by comparison with existing gridded datasets of Antarctica, and this finding is likely transferable to other cavities in Dronning Maud Land (Smith et al., 2020). To validate the source of super-cooled water, leading to platelet ice formation, and subsequent advection processes, a detailed examination of Conductivity, Temperature, and Depth (CTD) data that is required. Specifically, these data will allow a closer look at ISW outflow areas is required to determine whether the thick SIPL is a result of redistribution or of enhanced ISW outflow in that specific location.

5. Conclusions

In this study, we conducted a comprehensive analysis of an extensive multi-frequency electromagnetic (EM) induction sounding dataset over Antarctic fast-ice with an underlying SIPL. The data were inverted with a newly available open-source inversion scheme to calculate fast-ice and platelet-layer thicknesses and conductivities.

Our findings demonstrate the feasibility of high-resolution mapping of platelet-layer thickness for extensive areas. The good spatial coverage revealed for the first time accumulation patterns and will enable identification of ice-shelf water outflow regions, emphasizing the potential for understanding sub-ice shelf processes and their potential changes in the future. Our methodology represents a crucial advancement in studying ocean/ice-shelf interactions with non-destructive EM methods. Complementary oceanographic measurements are still required to attribute accumulation regions either to enhanced accumulation from redistribution of platelet ice or to enhanced supply by Ice Shelf Water (ISW) outflow.

Significantly, this investigation stands out as the first study encompassing the entirety of Atka Bay, including the ice shelf fringes. This surpasses the constraints of previous studies that omitted the mapping of these crucial areas, where ISW outflow can occur. Adapting the present methodology to airborne multi-frequency EM measurements could further extend spatial coverage, either by drones using GEM-2 s, or by aircraft using EM birds.

Our results indicate that a straightforward calibration involving offsets in a zero-conductivity environment yields reliable outcomes compared to drill holes. This calibration approach reduces logistical efforts and time constraints while addressing electronic offsets and drift over time. Furthermore, we demonstrated the the noise characteristics of the GEM-2 instrument on a sledge towed by a snowmobile allow for obtaining SIPL thickness with an accuracy of better than 20 cm within the common thickness range of 1 to 8 m and realistic instrument motion. This finding underscores the robustness of our approach in capturing fine details of the platelet layer distributions, contributing valuable insights to the understanding of Antarctic fast-ice regimes.

CRediT authorship contribution statement

Mara Neudert: Writing – review & editing, Writing – original draft, Visualization, Validation, Software, Methodology, Investigation, Formal analysis, Data curation, Conceptualization. **Stefan Hendricks:** Writing – review & editing, Supervision, Software, Methodology, Conceptualization. **Mario Hoppmann:** Writing – review & editing, Conceptualization. **Markus Schulze:** Investigation, Conceptualization. **Christian Haas:** Writing – review & editing, Supervision, Resources, Conceptualization.

Declaration of competing interest

The authors declare that they have no conflict of interest.

Data availability

The data are publicly accessible via the following DOIs: https://doi.org/10.1594/PANGAEA.968459 - Thickness and properties of sea ice and snow of land-fast sea ice in Atka Bay in November and December 2022. https://doi.org/10.1594/PANGAEA.968041 - Preliminary DOI for GEM-2 ice and platelet total thickness measurements from the 2022–2023 AFIN summer campaign.

Acknowledgements

Funding Support: This work was supported by the Alfred-Wegener-Institut, Helmholtz-Zentrum für Polar- und Meeresforschung, the German Research Foundation's (DFG) projects fAntasie (AR1236/3-1) and SnowCast (AR1236/1-1) within its priority program "Antarctic Research with comparative investigations in the Arctic ice areas" (SPP1158), and the DFG Emmy Noether Programme project SNOWflAke (project number 493362232).

We are most grateful for the logistics support and infrastructure provided by AWI and the welcoming staff at Neumayer III Station. We particularly thank Jölund Asseng and the wintering crews of the 42nd and 43rd wintering for excellent field support and their team efforts contributing to the AFIN monitoring program: Markus Schulze, Karsten

Böddeker, Werner Hofmann, Aurelia Hölzer, Hannes Keck, Alicia Rohnacher, Michael Trautmann, Benita Wagner, Katrin Wiggins and Lukas Ole Muser, Martin Radenz, Markus Ayasse, Peter Frölich, Martin Grabbert, Eva Link, Nora Schoeder, Felix Strobel, Bernd Wondratschek and Nellie Wullenweber. We extend our gratitude to Horst Bornemann, Christoph Held, and Henning Schröder for stimulating discussions about platelet layer properties through their valuable insights gained from ROV camera dives conducted in 2022/23.

Appendix A. Model studies with synthetic data

To find a fast and reliable inversion method, we tested different algorithms implemented in SciPy and available in EMagPy (McLachlan et al., 2021), utilizing the Hankel transform calculated by linear filtering (Guptasarma and Singh, 1997; Anderson, 1979) to solve the forward model provided by Wait (1982). We modified the responses to a layered earth (Wait, 1982) used as forward models in the framework of EMagPy by making the real part, the Inphase, available, including the bucking coil as a second receiver according to Hunkeler et al. (2016a), and adding all SciPy algorithms as solvers for the inverse problem.

We generated synthetic data for a set of 1D models, simulating field conditions by incorporating our standard frequency setup and instrument-specific parameters. The models considered three-layer structures: an ice+snow layer with a conductivity of 50 mS/m and thicknesses ranging from 0.5 to 5 m (in increments of 0.25 m), a SIPL with a conductivity of 850 mS/m and thicknesses ranging from 0.5 to 10 m (in increments of 0.25 m), and a seawater layer with a conductivity of 2700 mS/m. To enhance the realism of the simulated data, we introduced Gaussian noise corresponding to 2.5 %. Subsequently, we conducted inversions on the synthetic data points.

A.1. Algorithm selection

In our algorithm selection process, the initial model (A1) consists of a first layer representing ice+snow, characterized by a thickness (conductivity) of 3 m (50 mS/m), a second layer representing the SIPL with a thickness (conductivity) of 5 m (850 mS/m), and a homogeneous half space with a conductivity of 2700 mS/m, representing the seawater below. During inversions using the Sequential Least Squares Programming (SLSQP) algorithm (Kraft, 1988), the %RMSE remained consistently below 5. The Nelder-Mead algorithm (Nelder and Mead, 1965) exhibited an average difference of 10.7 in the inverted SIPL thickness compared to the true thickness. This difference was only marginally higher for the SLSQP algorithm, recording 11.6. To show the impact of the error on the most important inverted property, namely the SIPL thickness, Fig. A1 shows the normalized difference between true and inverted SIPL thickness for different minimization algorithms. The ice+snow and SIPL thickness ranges encountered in the field are delineated by the dashed box.

Results for other free parameters obtained through the Nelder-Mead algorithm were comparable to those obtained with SLSQP, albeit with a threefold increase in computing time. The L-BFGS-B and TNC algorithms did not consistently achieve acceptable errors across most data. Consequently, we have chosen the SLSQP algorithm for all subsequent inversions due to its consistently reliable performance.

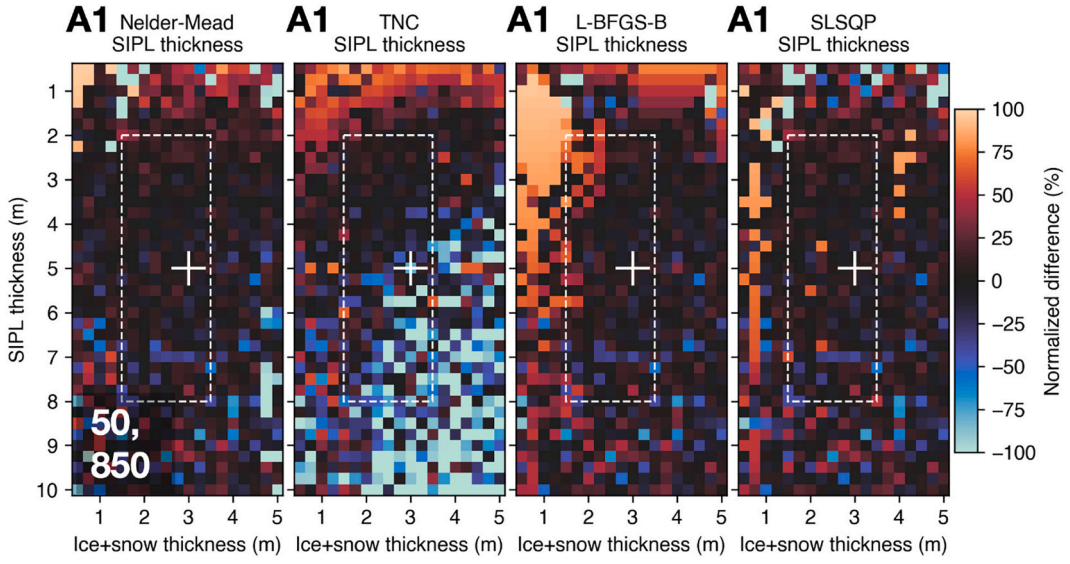

Fig. A1. Normalized difference between synthetic (true) model and inversion results, respectively for the inverted SIPL thickness for various combinations of sea-ice (0.5–5 m) and SIPL (0.5–10 m) thicknesses inverted with different algorithms. True ice+snow, SIPL and seawater conductivities were 50 mS/m, 850 mS/m and 2700 mS/m, respectively. Inversions were performed with a starting model according to (A1), starting depths marked by the cross. Dark colors indicate a very good agreement between inverted and true thickness, while red and blue represent over- and underestimations of the inversion results compared to the true subsurface model. (For interpretation of the references to colour in this figure legend, the reader is referred to the web version of this article.)

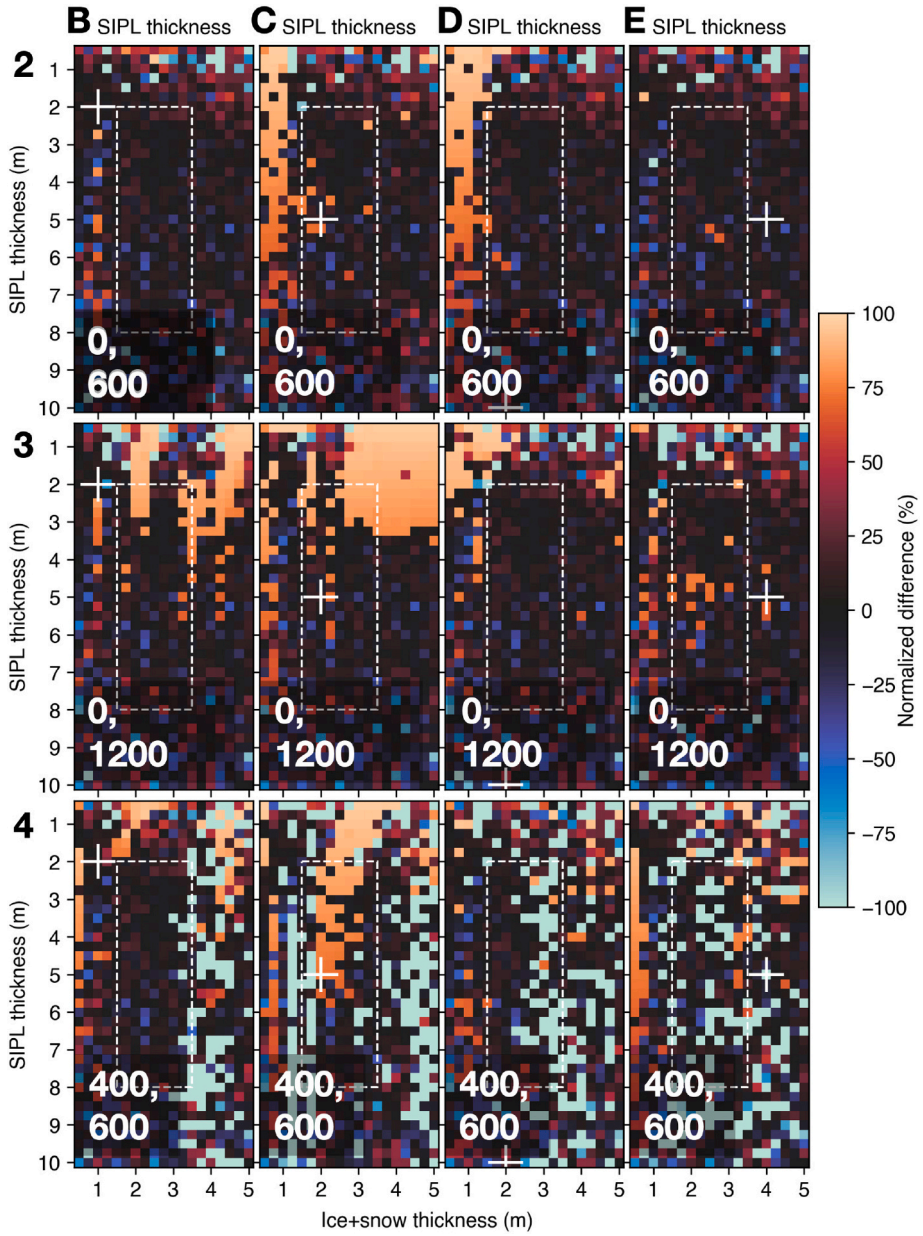

Fig. A2. Normalized differences of SIPL thickness between synthetic (true) model and inversion results for various combinations of sea-ice (0.5–5 m) and SIPL (0.5–10 m) thicknesses. True sea-ice, SIPL and seawater conductivities were 50 mS/m, 850 mS/m and 2700 mS/m, respectively. Inversions were performed with a starting model according to ice+snow and SIPL conductivities (in mS/m) of 2) 0 and 600, 3) 0 and 1200, 4) 400 and 600; and ice+snow and SIPL depths (in m) of B) 1 and 2, C) 2 and 10, D) 4 and 5. Dark colors indicate a very good agreement between modeled and true thickness (conductivity), while red and blue colors represent over- and underestimations of the inversion results compared to the true model, respectively. (For interpretation of the references to colour in this figure legend, the reader is referred to the web version of this article.)

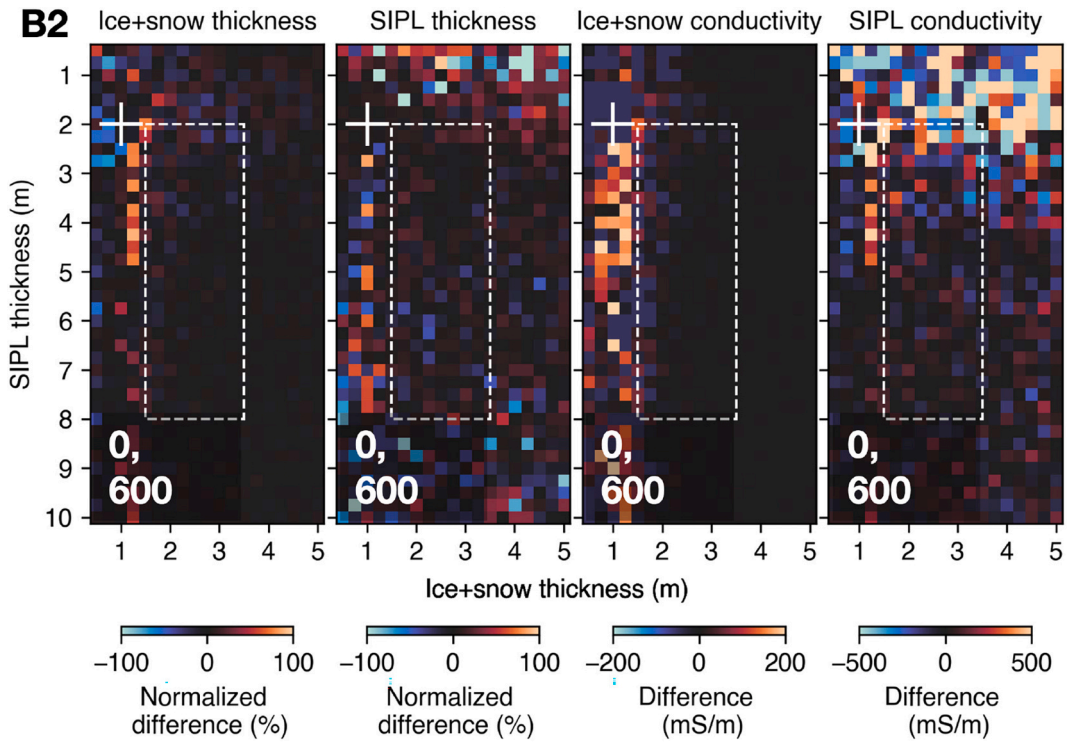

Fig. A3. Normalized differences between synthetic (true) model and inversion results for various combinations of sea-ice (0.5–5 m) and SIPL (0.5–10 m) thicknesses. True sea-ice, SIPL and seawater conductivities were 50 mS/m, 850 mS/m and 2700 mS/m, respectively. Inversion was performed with a starting model according to ice+snow and SIPL thicknesses of 1 and 2 m (cell B2 in Fig. A2). The starting conductivities (in mS/m) are 2) 0 and 600.

A.2. Starting model selection

To assess the impact of the starting model on the SLSQP performance, we conducted repeated inversions of synthetic data with 12 variations of slightly modified initial models. These variations included different depths (in meters) for the initial ice+snow and SIPLs:

A. 1 and 2,
B. 2 and 5,
C. 2 and 10,
D. 4 and 5, respectively.

Additionally, variations in the initial conductivities (in mS/m) for the ice+snow and SIPLs were considered:

1. 0 and 600,
2. 0 and 1200,
3. 400 and 600, respectively.

The normalized differences between the inversion results and the synthetic (true) data for the four free parameters across the 12 different starting models are exemplified for the SIPL thickness in Fig. A2.

The optimal starting model, identified as B2, had starting conductivities of 0 mS/m and 600 mS/m, along with starting depths of 1 and 2 m. In this scenario, the inversion results for each free parameter are depicted in Fig. S3. The calculated ice+snow thicknesses and SIPL thicknesses (Fig. A3, first two columns) generally agreed well with the true values within ± 10 %. The SIPL conductivity (Fig. A3, last column) was also well reproduced (± 10 %), except for thin SIPL thickness (below 2.5 m), where the conductivity was underestimated. Given the infrequent observation of SIPL thicknesses below 2.5 m, the inversion algorithm demonstrates reliability within these limits. However, sea ice thickness resolution was limited for ice thinner than 1.5 m.

Appendix B. Tables

B.1. Mean thickness from drill holes

Table B1. Overview of the drill hole transect mean±standard deviation of snow, consolidated ice, and SIPL thickness.

Date	Transect	No. of stations	Drill holes per station	Snow (m)	Consolidated ice (m)	SIPL (m)
2022-10-27	ATKA standard	5	5	0.50 (0.38)	2.20 (0.46)	3.56 (0.64)
2022-11-05	ATKA SNw	8	5	0.73 (1.04)	1.97 (0.15)	3.97 (0.62)
2022-11-07	ATKA SNe	7	5	0.53 (0.38)	1.91 (0.22)	5.44 (1.44)
2022–11–12	ATKA parallel	5	5	0.34 (0.29)	2.12 (0.25)	4.88 (0.88)
2022–11–16	ATKA standard	5	5	0.49 (0.33)	2.11 (0.22)	4.30 (0.67)
2022-12-13	ATKA SNw	7	3	0.48 (0.39)	2.34 (0.56)	4.11 (0.79)
2022-12-26	ATKA standard	3	5	0.61 (0.34)	2.10 (0.12)	3.36 (0.55)

B.2. Inversion results for different distributions of signal noise

Table B2. Inversion results (mean ± standard deviation) for each station on the transect of 16 Nov. The underlying noise distributions are either the measured instrument noise when the instrument was stationary (random) or modeled noise from rolling motion (motion).

Site	Noise	Ice+snow thickness	SIPL thickness	SIPL conductivity
		(m)	(m)	(mS/m)
ATKA03	random	2.57 ± 0.03	3.61 ± 0.09	804 ± 20
	motion	2.59 ± 0.02	3.64 ± 0.07	799 ± 9
ATKA07	random	2.56 ± 0.02	4.02 ± 0.11	941 ± 16
	motion	2.57 ± 0.02	4.05 ± 0.07	934 ± 11
ATKA11	random	2.97 ± 0.02	4.07 ± 0.13	1009 ± 19
	motion	2.99 ± 0.02	4.09 ± 0.07	1001 ± 13
ATKA16	random	2.91 ± 0.02	4.31 ± 0.12	965 ± 19
	motion	2.92 ± 0.02	4.34 ± 0.07	957 ± 12
ATKA21	random	1.90 ± 0.08	4.38 ± 0.07	452 ± 17
	motion	1.91 ± 0.00	4.41 ± 0.06	447 ± 7
ATKA24	random	2.25 ± 0.02	3.16 ± 0.07	1030 ± 22
	motion	2.26 ± 0.02	3.19 ± 0.06	1023 ± 11

B.3. Filtering of inversion results

Table B3. Percentage of data excluded due to post-inversion filtering criteria. lt = lower threshold (0.51 m for ice+snow thickness, 0.51 m for SIPL thickness, 401 mS/M for SIPL conductivity). ut = upper threshold (15 m for ice+snow, 15 m for SIPL, 1799 mS/m for SIPL conductivity), ls = lateral smoothness constraint (2 m deviation for ice+snow, 2 m deviation for SIPL), total = total percentage of remaining data.

Date	Ice+snow thickness			SIPL thickness			SIPL cond	SIPL thickness	%RMSE	total
Date	lt	ut	ls	lt	ut	ls	lt	ut	> 10	%
2022-10-27	5.8	5.8	5.8	5.8	32	38.3	6.9	5.8	5.8	61.6
2022-11-05	4.2	4.2	4.2	4.2	10.7	16.2	8.2	4.7	4.2	83.8
2022-11-08	0.7	0.7	0.7	0.7	14.1	28.4	14	0.7	2.7	71.6
2022–11–11	0.4	0.4	0.4	0.4	2.4	9.5	4.2	3.7	0.5	90.5
2022–11–12	1.3	1.3	1.3	1.3	8.9	20	10.6	1.3	1.5	80
2022–11–16	0.5	0.5	0.5	0.5	1.1	5.3	4.6	0.5	0.5	94.7
2022–11–19	3.1	3.1	3.1	3.1	17.5	23.1	6.4	3.1	3.1	76.9
2022-11-20	0.1	0.1	0.1	0.1	7.1	24.2	16.1	0.1	0.1	75.8
2022-11-22	1.8	1.8	1.8	1.8	10	24.6	14.9	1.8	2.1	75.4
2022-11-23	28	28	28	28	34.1	35.6	28.5	28	28	64.4
2022-12-04	2	2	2	2	10.5	15.3	3.3	2	2.3	84.7
2022-12-05	0.3	0.3	0.3	0.3	1.3	4.5	3.4	0.3	0.3	95.5
2022-12-06	0.7	0.7	0.7	0.7	5.2	10.1	4.7	0.9	0.9	89.9
2022-12-12	34.6	34.6	34.6	34.6	50	59.7	39.5	34.7	34.7	40.3
2022-12-13	1.1	1.1	1.1	1.1	3.8	20.4	17.2	1.9	2	79.5
2022-12-14	0.1	0.1	0.1	0.1	1.8	12.2	10.3	0.1	0.2	87.8
2022-12-15	0.9	0.9	0.9	0.9	8.5	32.8	23.3	0.9	1	67.2
2022-12-17	0	0	0	0	6.2	16.1	8.1	0	0.1	83.8
2022-12-23	20.5	20.5	20.5	20.5	21.8	26.8	25.3	20.5	20.5	73.2
2022-12-25	0.8	0.6	0.8	0.8	3.5	10.2	6.4	0.6	1.6	89.3
2022-12-26	0.3	0.3	0.3	0.3	0.6	18.3	18	0.3	0.3	81.7

(continued on next page)

(*continued*)

Date	Ice+snow thickness			SIPL thickness			SIPL cond	SIPL thickness	%RMSE	total
Date	lt	ut	ls	lt	ut	ls	lt	ut	> 10	%
2022-12-30	0	0	0	0	0.4	4.7	4.3	0.1	0.1	95.2
2022-12-31	0.7	0.7	0.7	0.7	2.8	7.9	5.4	0.7	0.7	92.1
2023-01-01	0.3	0.3	0.3	0.3	1.7	7.8	6.1	0.3	0.3	92.2
2023-01-03	0	0	0	0	7.8	16.3	6	0.1	0.1	83.7

References

Anderson, W.L., 1979. Computer program; numerical integration of related Hankel transforms of orders O and 1 by adaptive digital filtering. Geophysics 44, 1287–1305. https://doi.org/10.1190/1.1441007.

Arndt, S., Hoppmann, M., Schmithüsen, H., Fraser, A.D., Nicolaus, M., 2020. Seasonal and interannual variability of landfast sea ice in Atka Bay, Weddell Sea, Antarctica. Cryosphere 14, 2775–2793. https://doi.org/10.5194/tc-14-2775-2020.

Brett, G.M., Irvin, A., Rack, W., Haas, C., Langhorne, P.J., Leonard, G.H., 2020. Variability in the distribution of Fast Ice and the Sub-ice Platelet Layer near McMurdo Ice Shelf. J. Geophys. Res. Oceans 125. https://doi.org/10.1029/2019JC015678 e2019JC015 678.

Brodie, R., Sambridge, M., 2006. A holistic approach to inversion of frequency-domain airborne EM data. Geophysics 71, G301–G312.

Crocker, G.B., 1988. Physical Processes in Antarctic Landfast Sea Ice. Ph.D. thesis. University of Cambridge.

Dorschel, B., Hehemann, L., Viquerat, S., Warnke, F., Dreutter, S., Tenberge, Y.S., Accettella, D., An, L., Barrios, F., Bazhenova, E., Black, J., Bohoyo, F., Davey, C., De Santis, L., Dotti, C.E., Fremand, A.C., Fretwell, P.T., Gales, J.A., Gao, J., Gasperini, L., Greenbaum, J.S., Jencks, J.H., Hogan, K., Hong, J.K., Jakobsson, M., Jensen, L., Kool, J., Larin, S., Larter, R.D., Leitchenkov, G., Loubrieu, B., Mackay, K., Mayer, L., Millan, R., Morlighem, M., Navidad, F., Nitsche, F.O., Nogi, Y., Pertuisot, C., Post, A. L., Pritchard, H.D., Purser, A., Rebesco, M., Rignot, E., Roberts, J.L., Rovere, M., Ryzhov, I., Sauli, C., Schmitt, T., Silvano, A., Smith, J., Snaith, H., Tate, A.J., Tinto, K., Vandenbossche, P., Weatherall, P., Wintersteller, P., Yang, C., Zhang, T., Arndt, J.E., 2022. The International Bathymetric Chart of the Southern Ocean Version 2. Scientific Data 9, 275. https://doi.org/10.1038/s41597-022-01366-7.

Fitterman, D.V., Yin, C., 2004. Effect of bird maneuver on frequency-domain helicopter EM response. Geophysics 69, 1203–1215. https://doi.org/10.1190/1.1801937.

Garmin Ltd, 2024. GPS 18x Technical Specifications. Garmin Ltd, Olathe, Kansas, USA document No. 190–00879-08_0F.

Gough, A.J., Mahoney, A.R., Langhorne, P.J., Williams, M.J., Robinson, N.J., Haskell, T. G., 2012. Signatures of supercooling: McMurdo Sound platelet ice. J. Glaciol. 58, 38–50. https://doi.org/10.3189/2012JoG10J218.

Guillemoteau, J., Sailhac, P., Behaegel, M., 2015. Modelling an arbitrarily oriented magnetic dipole over a homogeneous half-space for a rapid topographic correction of airborne EM data. Explor. Geophys. 46, 85–96. https://doi.org/10.1071/EG13093.

Günther, S., Dieckmann, G.S., 1999. Seasonal development of algal biomass in snow-covered fast ice and the underlying platelet layer in the Weddell Sea, Antarctica. Antarct. Sci. 11, 305–315. https://doi.org/10.1017/S0954102099000395.

Guptasarma, D., Singh, B., 1997. New digital linear filters for Hankel J0 and J1 transforms. Geophys. Prospect. 45, 745–762. https://doi.org/10.1046/j.1365-2478.1997.500292.x.

Haas, C., Gerland, S., Eicken, H., Miller, H., 1997. Comparison of sea-ice thickness measurements under summer and winter conditions in the Arctic using a small electromagnetic induction device. Geophysics 62, 749–757. https://doi.org/10.1190/1.1444184.

Haas, C., Langhorne, P.J., Rack, W., Leonard, G.H., Brett, G.M., Price, D., Beckers, J.F., Gough, A.J., 2021. Airborne mapping of the sub-ice platelet layer under fast ice in McMurdo Sound, Antarctica. Cryosphere 15, 247–264. https://doi.org/10.5194/tc-15-247-2021.

Holladay, J., Lo, B., Prinsenberg, S., 1997. Bird orientation effects in quantitative airborne electromagnetic interpretation of pack ice thickness sounding. In: Oceans '97. MTS/IEEE Conference Proceedings, vol. 2, pp. 1114–1119. https://doi.org/10.1109/OCEANS.1997.624148.

Hoppmann, M., Nicolaus, M., Asseng, J., 2012. Summary of AFIN Measurements on Atka Bay Landfast Seea Ice in 2011.

Hoppmann, M., Nicolaus, M., Hunkeler, P.A., Heil, P., Behrens, L.-K., König-Langlo, G., Gerdes, R., 2015a. Seasonal evolution of an ice-shelf influenced fast-ice regime, derived from an autonomous thermistor chain. J. Geophys. Res. Oceans 120, 1703–1724. https://doi.org/10.1002/2014JC010327.

Hoppmann, M., Nicolaus, M., Paul, S., Hunkeler, P.A., Heinemann, G., Willmes, S., Timmermann, R., Boebel, O., Schmidt, T., Kühnel, M., et al., 2015b. Ice platelets below Weddell Sea landfast sea ice. Ann. Glaciol. 56, 175–190. https://doi.org/10.3189/2015AoG69A678.

Hoppmann, M., Richter, M.E., Smith, I.J., Jendersie, S., Langhorne, P.J., Thomas, D.N., Dieckmann, G.S., 2020. Platelet ice, the Southern Ocean's hidden ice: a review. Ann. Glaciol. 61, 341–368. https://doi.org/10.1017/aog.2020.54.

Hunkeler, P., Hendricks, S., Hoppmann, M., Farquharson, C., Kalscheuer, T., Grab, M., Kaufmann, M.S., Rabenstein, L., Gerdes, R., 2016a. Improved 1D inversions for sea ice thickness and conductivity from electromagnetic induction data: inclusion of nonlinearities caused by passive bucking. GEOPHYSICS 81. https://doi.org/10.1190/GEO2015-0130.1. WA45–WA58.

Hunkeler, P.A., Hendricks, S., Hoppmann, M., Paul, S., Gerdes, R., 2015. Towards an estimation of sub-sea-ice platelet-layer volume with multi-frequency electromagnetic induction sounding. Ann. Glaciol. 56, 137–146. https://doi.org/10.3189/2015AoG69A705.

Hunkeler, P.A., Hoppmann, M., Hendricks, S., Kalscheuer, T., Gerdes, R., 2016b. A glimpse beneath Antarctic Sea ice: Platelet layer volume from multifrequency electromagnetic induction sounding. Geophys. Res. Lett. 43, 222–231. https://doi.org/10.1002/2015GL065074.

Jacobs, S.S., 2004. Bottom water production and its links with the thermohaline circulation. Antarct. Sci. 16, 427–437. https://doi.org/10.1017/S095410200400224X.

Jones, K.A., Ingham, M., Eicken, H., 2012. Modeling the anisotropic brine microstructure in first-year Arctic Sea ice. J. Geophys. Res. Oceans 117. https://doi.org/10.1029/2011JC007607.

Kraft, D., 1988. A Software Package for Sequential Quadratic Programming, Forschungsbericht- Deutsche Forschungs- und Versuchsanstalt fur Luft- und Raumfahrt.

Langhorne, P.J., Hughes, K.G., Gough, A.J., Smith, I.J., Williams, M.J.M., Robinson, N.J., Stevens, C.L., Rack, W., Price, D., Leonard, G.H., Mahoney, A.R., Haas, C., Haskell, T. G., 2015. Observed platelet ice distributions in Antarctic Sea ice: An index for ocean-ice shelf heat flux. Geophys. Res. Lett. 42, 5442–5451. https://doi.org/10.1002/2015GL064508.

Mahoney, A.R., Gough, A.J., Langhorne, P.J., Robinson, N.J., Stevens, C.L., Williams, M. M., Haskell, T.G., 2011. The seasonal appearance of ice shelf water in coastal Antarctica and its effect on sea ice growth. J. Geophys. Res. Oceans 116.

Martinelli, P., Duplaá, M.C., 2008. Laterally filtered 1D inversions of small-loop, frequency-domain EMI data from a chemical waste site. GEOPHYSICS 73, F143–F149. https://doi.org/10.1190/1.2917197.

McLachlan, P., Blanchy, G., Binley, A., 2021. EMagPy: Open-source standalone software for processing, forward modeling and inversion of electromagnetic induction data. Comput. Geosci. 146, 104–561. https://doi.org/10.1016/j.cageo.2020.104561.

Minsley, B.J., Smith, B.D., Hammack, R., Sams, J.I., Veloski, G., 2012. Calibration and filtering strategies for frequency domain electromagnetic data. J. Appl. Geophys. 80, 56–66. https://doi.org/10.1016/j.jappgeo.2012.01.008.

Nelder, J.A., Mead, R., 1965. A simplex method for function minimization. Comput. J. 7, 308–313.

Reid, J.E., Worby, A.P., Vrbancich, J., Munro, A.I.S., 2003. Shipborne electromagnetic measurements of Antarctic Sea-ice thickness. GEOPHYSICS 68, 1537–1546. https://doi.org/10.1190/1.1620627.

Robinson, N.J., Williams, M.J.M., Stevens, C.L., Langhorne, P.J., Haskell, T.G., 2014. Evolution of a supercooled Ice Shelf Water plume with an actively growing subice platelet matrix. J. Geophys. Res. Oceans 119, 3425–3446. https://doi.org/10.1002/2013JC009399.

Smith, E.C., Hattermann, T., Kuhn, G., Gaedicke, C., Berger, S., Drews, R., Ehlers, T.A., Franke, D., Gromig, R., Hofstede, C., et al., 2020. Detailed seismic bathymetry beneath Ekström Ice Shelf, Antarctica: implications for glacial history and ice-ocean interaction. Geophys. Res. Lett. 47. https://doi.org/10.1029/2019GL086187 e2019GL086 187.

Timco, G., Weeks, W., 2010. A review of the engineering properties of sea ice. Cold Reg. Sci. Technol. 60, 107–129. https://doi.org/10.1016/j.coldregions.2009.10.003.

Vilhelmsen, T.B., Døssing, A., 2022. Drone-towed controlled-source electromagnetic (CSEM) system for near-surface geophysical prospecting: on instrument noise, temperature drift, transmission frequency, and survey set-up. Geosci. Instrument. Methods Data Syst. 11, 435–450. https://doi.org/10.5194/gi-11-435-2022.

Wait, J.R., 1982. Chapter III - Electromagnetic Induction and Loop–Loop Coupling. In: Wait, J.R. (Ed.), Geo-Electromagnetism. Academic Press, pp. 101–139. https://doi.org/10.1016/B978-0-12-730880-7.50007-7.

Werthmüller, D., 2017. An open-source full 3D electromagnetic modeler for 1D VTI media in Python: Empymod. Geophysics 82. https://doi.org/10.1190/GEO2016-0626.1. WB9–WB19.

Wongpan, P., Langhorne, P.J., Dempsey, D.E., Hahn-Woernle, L., Sun, Z., 2015. Simulation of the crystal growth of platelet sea ice with diffusive heat and mass transfer. Ann. Glaciol. 56, 127–136. https://doi.org/10.3189/2015AoG69A777.

Wongpan, P., Vancoppenolle, M., Langhorne, P.J., Smith, I.J., Madec, G., Gough, A.J., Mahoney, A.R., Haskell, T., 2021. G.: Sub-Ice Platelet Layer Physics: Insights from a Mushy-Layer Sea Ice Model. J. Geophys. Res. Oceans 126. https://doi.org/10.1029/2019JC015918 e2019JC015 918.

Wu, S., Huang, Q., Zhao, L., 2023. Fast Bayesian inversion of airborne electromagnetic data based on the Invertible Neural Network. IEEE Trans. Geosci. Remote Sens. 61, 1–11. https://doi.org/10.1109/TGRS.2023.3264777.

Yin, C., Fraser, D.C., 2004. Attitude corrections of helicopter EM data using a superposed dipole model. Geophysics 69, 431–438. https://doi.org/10.1190/1.1707063.

Zaru, N., Silvestri, S., Assiri, M., Bai, P., Hansen, T.M., Vignoli, G., 2024. Probabilistic petrophysical reconstruction of Danta's Alpine Peatland via electromagnetic Induction Data, Earth and Space. Science 11. https://doi.org/10.1029/2023EA003457 e2023EA003457.